Neuron

Article

Multipotent progenitors instruct ontogeny of the superior colliculus

Graphical abstract

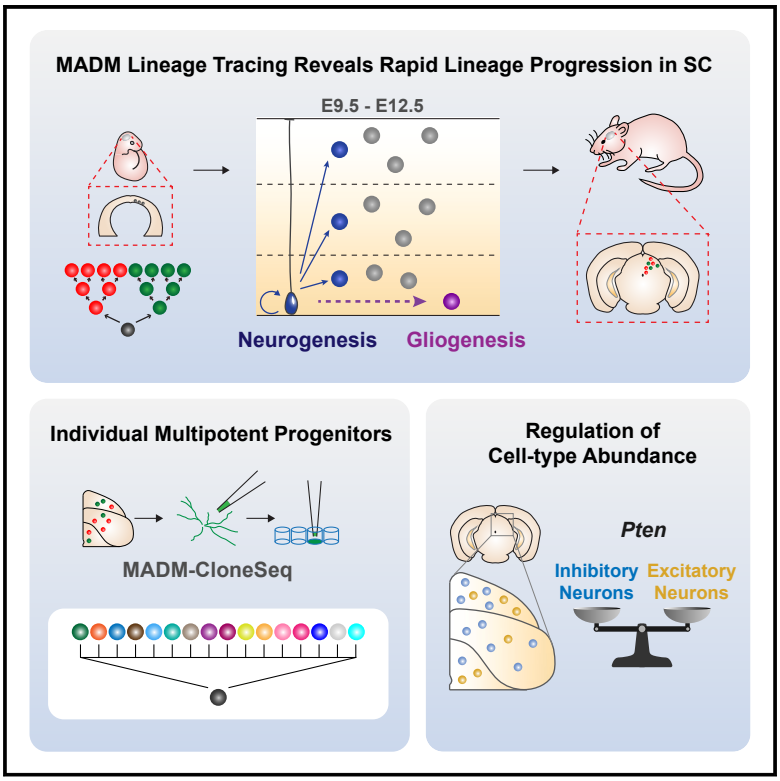

Highlights

- SC cell-type diversity originates from a single common pool of progenitors
- Rapid RGP lineage progression without temporal order of layer production in SC
- Individual RGPs are multipotent with the capacity to generate all SC neuronal types
- Cell-autonomous requirement of *Pten* for the establishment of SC cell-type diversity

Authors

Giselle Cheung, Florian M. Pauler, Peter Koppensteiner, ..., Christoph Bock, Ryuichi Shigemoto, Simon Hippenmeyer

Correspondence

simon.hippenmeyer@ist.ac.at

In brief

Cheung et al. combine MADM-based lineage tracing with single-cell RNA sequencing to uncover the ontogenetic framework of the mouse superior colliculus. Individual progenitors show an exceptional capacity to produce all known excitatory *and* inhibitory neuron types and thus overall neuronal cell-type diversity in superior colliculus in a PTEN-dependent manner.

Cheung et al., 2024, Neuron *112*, 230–246
January 17, 2024
https://doi.org/10.1016/j.neuron.2023.11.009

CellPress

CellPress
OPEN ACCESS

Neuron

Article

Multipotent progenitors instruct ontogeny of the superior colliculus

Giselle Cheung,[1,5] Florian M. Pauler,[1,5] Peter Koppensteiner,[1,5] Thomas Krausgruber,[2,3] Carmen Streicher,[1] Martin Schrammel,[1] Natalie Gutmann-Özgen,[1] Alexis E. Ivec,[1,4] Christoph Bock,[2,3] Ryuichi Shigemoto,[1] and Simon Hippenmeyer[1,6,*]

[1]Institute of Science and Technology Austria (ISTA), Am Campus 1, 3400 Klosterneuburg, Austria
[2]CeMM Research Center for Molecular Medicine, Austrian Academy of Sciences; 1090 Vienna, Austria
[3]Medical University of Vienna, Institute of Artificial Intelligence, Center for Medical Data Science, 1090 Vienna, Austria
[4]Present address: Department of Neurology and Neurological Sciences, Stanford University, USA
[5]These authors contributed equally
[6]Lead contact
*Correspondence: simon.hippenmeyer@ist.ac.at
https://doi.org/10.1016/j.neuron.2023.11.009

SUMMARY

The superior colliculus (SC) in the mammalian midbrain is essential for multisensory integration and is composed of a rich diversity of excitatory and inhibitory neurons and glia. However, the developmental principles directing the generation of SC cell-type diversity are not understood. Here, we pursued systematic cell lineage tracing *in silico* and *in vivo*, preserving full spatial information, using genetic mosaic analysis with double markers (MADM)-based clonal analysis with single-cell sequencing (MADM-CloneSeq). The analysis of clonally related cell lineages revealed that radial glial progenitors (RGPs) in SC are exceptionally multipotent. Individual resident RGPs have the capacity to produce all excitatory *and* inhibitory SC neuron types, even at the stage of terminal division. While individual clonal units show no pre-defined cellular composition, the establishment of appropriate relative proportions of distinct neuronal types occurs in a PTEN-dependent manner. Collectively, our findings provide an inaugural framework at the single-RGP/-cell level of the mammalian SC ontogeny.

INTRODUCTION

The mouse superior colliculus (SC) is located in the dorsal midbrain and is essential for multisensory integration, attention, arousal brain states, and motor responses required for complex behavior.[1–3] With six alternating strata of cell bodies and fibers, the superficial layers (sSC) are important for visual functions, receiving direct inputs from the retina, whereas the deep layers (dSC) are sites of auditory and somatosensory processing.[4–8] Recent research, mapping SC input/output connections with cortical areas,[9] demonstrated its role in segregating somatosensory and visual circuits[10] and has supported its critical contribution to complex neural processes across the brain. Indeed, SC dysfunction leads to deficits in sensory processing and has been implicated in neurodevelopmental diseases such as autism and attention deficit hypersensitive disorders.[11,12]

The faithful production and distribution of the diverse neuronal and glial cell types during development are fundamental to the establishment of the highly complex SC cytoarchitecture, laminar arrangement, and eventual circuit assembly. However, the cellular principles directing the generation of cell-type diversity and the overall ontogeny of the SC remain poorly understood. In fact, the origins of SC excitatory glutamatergic and inhibitory GABAergic neuronal populations remain obscure although glutamatergic and GABAergic progenitor domains are thought to overlap in the developing dorsal midbrain.[13–15] While pioneering studies have identified radial glial progenitors (RGPs) lining the ventricular surface in chick optic tectum, a non-mammalian vertebrate homolog of the SC,[16,17] and in the developing rodent midbrain,[4] their potential, proliferation behavior, and neurogenic and gliogenic output have not been investigated at the individual progenitor level.

The mature SC is composed of a rich variety of distinct neuron types that show highly variable morphology, receptive field sizes, physiological properties, and synaptic target areas.[1,2,4,9] Yet, most information related to SC cell-type diversity has been derived based on the physiological characteristics of a limited number of experimentally accessible cells, primarily located in the sSC.[18–22] Recent efforts have, however, commenced to systematically catalog cell types, based on single-cell transcriptome,[23–27] and thus provide an exciting starting point for our general understanding of the extent of SC cell-type diversity. Nonetheless, how cell-type diversity emerges from progenitors in the developing SC is not known. Here, we define

the developmental principles governing RGP cell lineage progression and the generation of cell-type diversity in SC at single-progenitor resolution.

RESULTS

A single common pool of progenitors in SC

In order to obtain a global overview of cell-type diversity and to temporally define *in silico* the emergence of neuronal cell types in the embryonic SC, we exploited a recent single-cell RNA sequencing (scRNA-seq) dataset[23] (Figure 1A). We extracted 26,532 dorsal midbrain-specific single cells of neuronal lineage from embryonic (E) 9–E18 time points (Figure S1A). Uniform manifold approximation and projection (UMAP), in combination with unsupervised clustering, identified a single continuum of cells including RGPs and immature and mature neurons (Figures 1B and S1B). RGPs were highly abundant at E9–E11 but sharply diminished by E12, coinciding with the peak of immature neuron abundance and the appearance of mature neurons (Figure 1C). Within the neuronal population, we identified two largely exclusive but continuous clusters of excitatory and inhibitory neurons, emerging simultaneously at E12 (Figures 1D, 1E, and S1B). The continuum of cells implied two distinct developmental trajectories from RGPs to neurons. Indeed, pseudotime analysis of the single-cell trajectory revealed connections from RGPs to mature neurons via immature neuronal states (Figure 1F). The trajectory graph also identified a number of endpoints that correlated well with our unsupervised clustering analysis (Figures S1C and S1D).

Next, we assessed how the transcriptional profile of nascent SC neurons correlates with their mature state. We performed label transfer from an adult dorsal midbrain scRNA-seq dataset[24] to the E18 dataset[23] (Figure 1G). From the adult dataset, we extracted 16 neuronal cell types (6 excitatory and 10 inhibitory subtypes) in the dorsal midbrain (Figures S1E and S1F). In our analysis, individual mature SC cell types were matched to broader but specific clusters of embryonic neurons (Figures 1H and 1I), indicating that a limited number of broad neuronal clusters in the embryo precipitates to all distinct mature SC cell types.

To test the hypothesis that all mature SC neuronal cell types emerge from a single population of RGPs, we gained experimental access to the RGP population in the developing SC via genetic means. We constructed a tamoxifen (TM)-inducible CreER driver line with transgene expression under the control of the *Frizzled-10* (*Fzd10*) promoter (*Fzd10-CreER*$^{+/-}$) and confirmed targeted expression in embryonic dorsal midbrain progenitors (Figures S2A–S2H). To more comprehensively assess the *Fzd10*-cell lineage, we crossed *Fzd10-CreER*$^{+/-}$ with the fluorescent *mTmG* reporter[28] (Figures S2I–S2K). We injected TM in *mTmG;Fzd10-CreER*$^{+/-}$ mice at E10.5 and collected and pooled GFP^{+} cells of the *Fzd10*-lineage at E12.5, E14.5, and E16.5 from the dorsal midbrain for scRNA-seq using 10× Genomics technology (Figure S2L). Our dataset including 5,552 high-quality *Fzd10*-lineage cells overlapped well with reference dataset[23] in the integrated UMAP and covered all midbrain-specific neuronal cell clusters in comparable proportions (Figures S2M–S2R). Thus, our *Fzd10*-CreER driver established in this study faithfully targets the relevant pools of embryonic RGPs, giving rise to cell lineages comprising all the distinct mature neuronal SC cell types.

Temporal lineage progression of SC progenitors

To precisely decipher the ontogeny of SC cell types from a single pool of RGPs, we next pursued clonal analysis by labeling individual RGPs and following their lineages (Figure 2A). We utilized mosaic analysis with double markers (MADM) technique to label individual units of clonally related cells.[29–32] MADM relies on CRE recombinase-mediated interchromosomal recombination in dividing RGPs, thereby labeling the two daughter cells and their respective progenies in distinct red (tdTomato [tdT]) or green (GFP) fluorescence (Figures 2B and S3A). Given the quantitative nature, MADM can provide optical readout of progenitor proliferation behavior at single-cell resolution. To specifically target the SC, we used MADM reporter cassettes on chromosome (chr) 11[30] with *Fzd10-CreER* driver.

We induced MADM clones at E9.5, E10.5, E11.5, or E12.5 in *MADM-11*$^{GT/TG}$*;Fzd10-CreER*$^{+/-}$ embryos and collected brains at postnatal day (P) 28-P30 (Figure S3B) for analysis (Figure 2C). We observed that SC MADM clones typically consisted of clusters of red and green neurons spanning across all layers of the adult SC and the periaqueductal gray (PAG) (Figures 2D and S3C–S3E). We analyzed 126 clones and observed that the neuronal output of individual progenitors, measured by clone size, decreased exponentially over a relatively short time window with considerable clone size variability at all induction time points (Figures 2E–2I and S4A–S4D). To independently validate and extend our dataset, we analyzed 142 clones induced with *Sox2*-CreER driver (uniformly expressed in neural stem and progenitor cells[33]). We noticed comparable neuronal output patterns in *MADM-11*$^{GT/TG}$*;Sox2*$^{CreER/+}$ brains corroborating our observations using *Fzd10-CreER*$^{+/-}$ (Figures 2J and S4E–S4H).

SC MADM clones showed "cone-shaped" architecture (Figures S5A–S5I) and a disproportionate layer distribution of neurons (34 ± 2% in sSC, 51 ± 2% in dSC, and 15 ± 2% in PAG; Figure 2K). The tangential dimension and overall dispersion of cells decreased significantly over time, resulting in narrower clones (Figures S5J–S5L). By contrast, the layer distribution of neurons (Figure 2K) and the radial dimension of the clones (Figure S5M) did not change over time. Thus, in contrast to other brain regions (e.g., neocortex), the emergence of laminae in SC did not follow a temporally stereotyped pattern.

Next, we determined the implicit cell division pattern of individual SC progenitors based on MADM subclone size. We analyzed clones induced at E9.5–E12.5 and classified all clones into three categories: (1) proliferative clones whereby the first division produced two self-renewing proliferative daughter cells, (2) asymmetric neurogenic clones where the minority clone consisted of a single postmitotic neuron and the other subclone of more than one cell, and (3) terminal neurogenic clones consisting of two single neurons labeled in distinct red/green colors (Figures 2L–2Q). The relative proportions of clone categories at each time point suggest that RGPs quickly shift from proliferative to terminal neurogenic mode (Figure 2R). Altogether, our MADM clonal analysis indicates that RGP lineage progression occurs

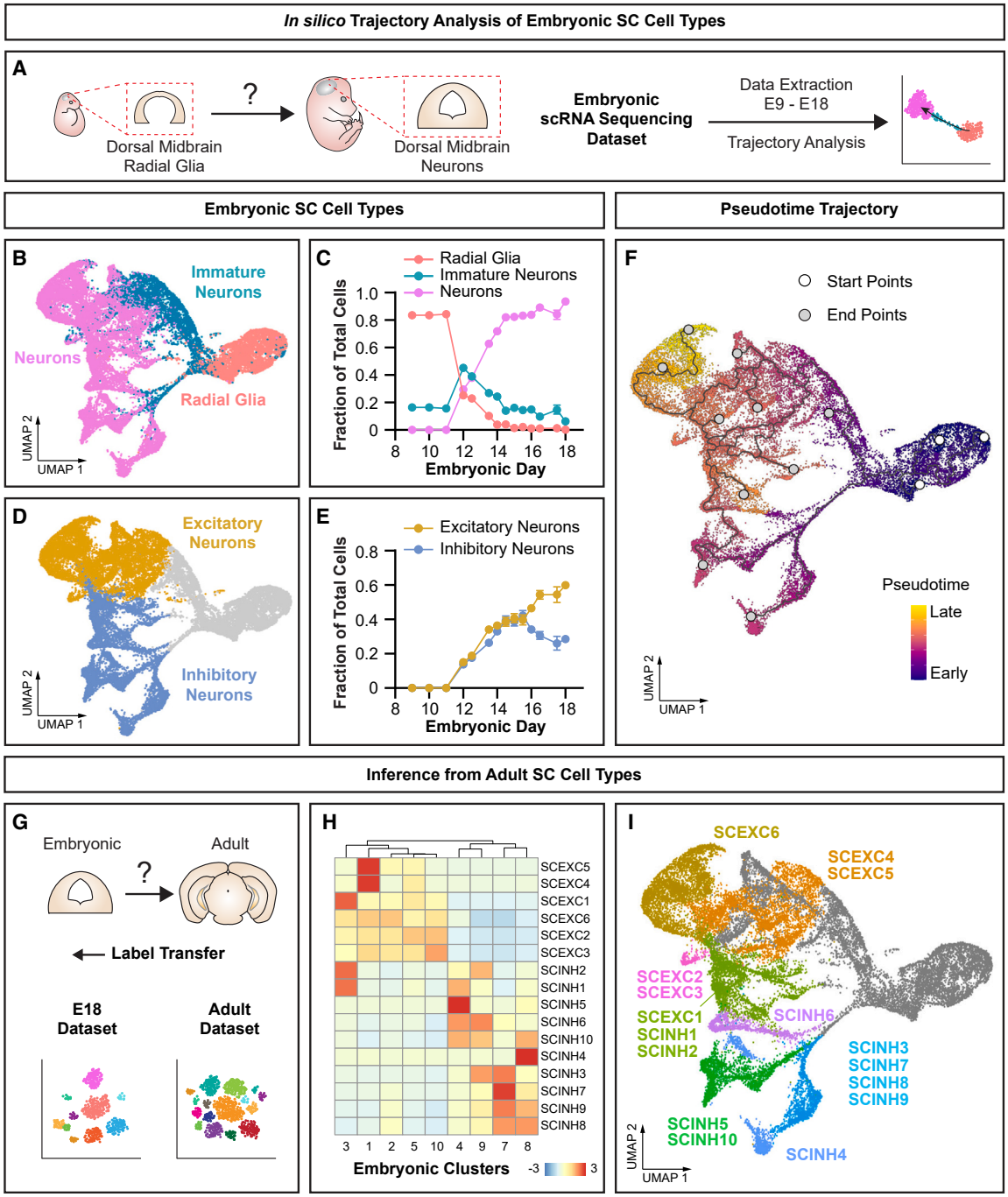

Figure 1. Emergence and developmental *in silico* trajectories of SC cell types

(A) Schematics illustrating the *in silico* analysis pipeline to assess the emergence of SC cell-type diversity during embryogenesis, based on embryonic reference dataset.[23]

(B–E) UMAPs and line plots of relative cell abundance (fraction ± 95% Clopper-Pearson confidence intervals) for distinct clusters of radial glia, immature and mature neurons (B and C), and excitatory and inhibitory neurons (D and E).

(F) UMAP with coloration indicating pseudotime. Developmental trajectory is indicated with corresponding start (white) and endpoints (gray).

(G) Schematics of label transfer analysis for inference from adult[24] to E18 reference datasets.

(H) Heatmap indicating the average similarity score of 9 embryonic neuronal clusters to 16 adult cell types extracted from adult reference.

(I) UMAP illustrating the most similar adult SC cell types matching to individual embryonic clusters, coloring of cells according to Figure S1C.

See also Figure S1.

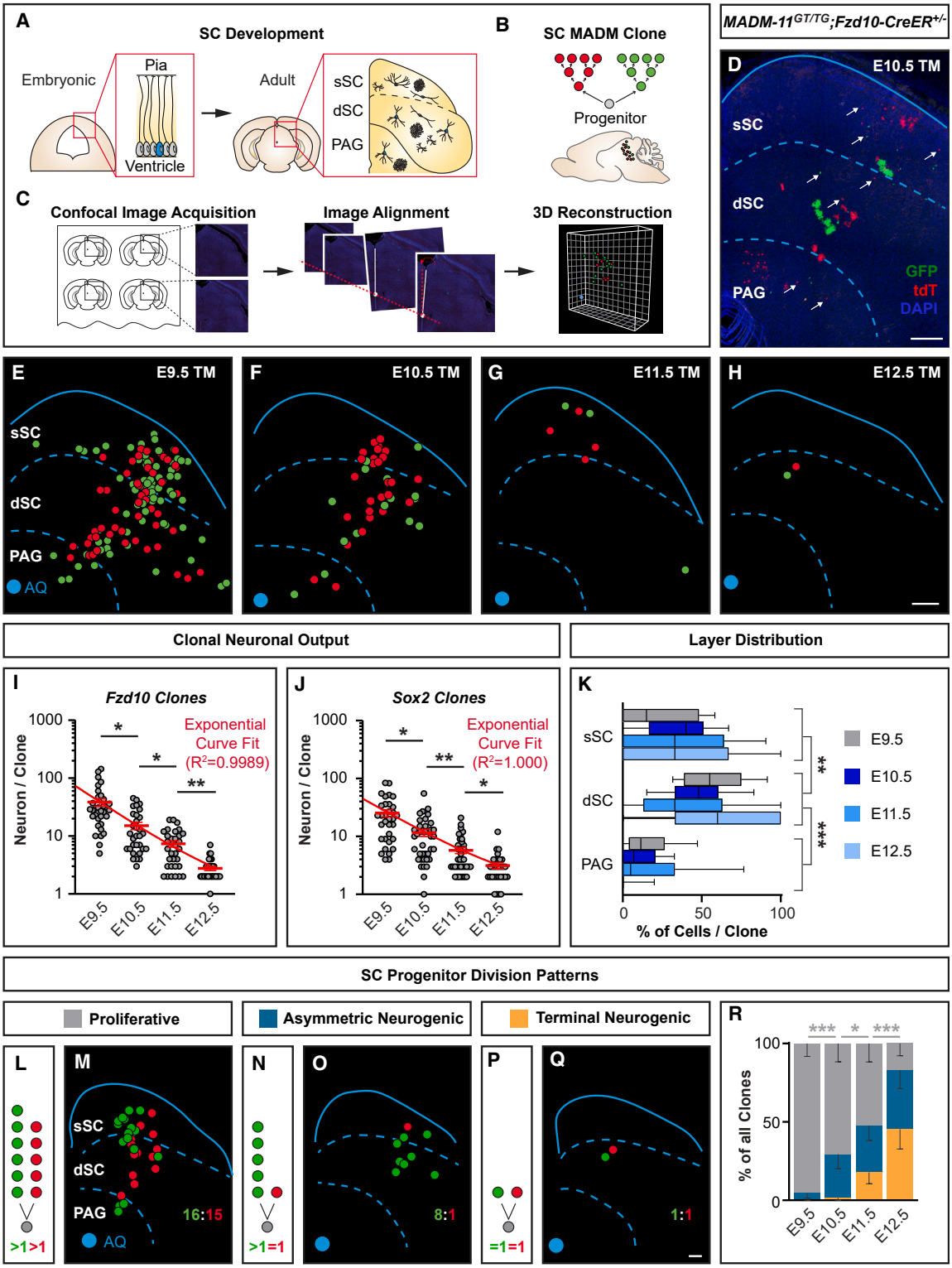

Figure 2. MADM clonal analysis reveals patterns of SC neurogenesis at single-progenitor level

(A–C) Schematics of the emergence of cell-type diversity during SC development (A); differentially labeled cell lineages in a MADM clone originating from an individual progenitor (B); and overview of image acquisition, alignment, and three-dimensional (3D) reconstruction of individual MADM clones (C).

(D) Representative maximum z-projected image of a MADM clone in SC, induced at E10.5 and collected at P28 in *MADM-11*$^{GT/TG}$*;Fzd10-CreER*$^{+/-}$. Red and green neurons are marked by white arrows. Protoplasmic astrocytes and small oligodendrocyte clusters are also visible.

(legend continued on next page)

rapidly in SC but that distinct laminae do not emerge in a temporally stereotyped pattern.

Glial production by individual SC progenitors

In addition to neurons, we also observed MADM labeling in two morphologically distinct populations of glial cells in SC MADM clones, namely astrocytes and oligodendrocytes (Figures S3F–S3G). Astrocytes displayed protoplasmic morphology and expressed SOX9, whereas oligodendrocytes were immunopositive for OLIG2 (Figures S3H–S3M). The presence of glia in SC clones confirmed that SC progenitors also generated glia in addition to neurons, consistent with earlier results in chick tectum.[34] However, the developmental programs mediating SC gliogenesis are still unclear. In order to address this issue, we extracted 1,819 glial progenitors from our reference [23] and found that they emerged from SC RGPs after E12 in the embryonic dorsal midbrain (Figure 3A). A combined UMAP of glial progenitors together with RGPs identified a continuum, indicating the development of glial progenitors from late (>E12) RGPs (Figures 3B–3D). We confirmed that glial progenitors were also present in the *Fzd10*-lineage (Figure 3E). Next, we proceeded with MADM clonal analysis to quantitatively assess SC gliogenesis.

Among 268 SC MADM neuron-containing clones used for neuronal clonal analysis, 152 (57%) also contained glia, which typically appeared in clusters (Figures 3F–3J). Importantly, we did not find any glia-only clones, suggesting that glial progenitors were not yet present before E12.5—consistent with our *in silico* analysis. While RGPs had a higher propensity to generate astrocytes than oligodendrocytes, clones containing both types were also observed (Figures 3F–3J). The potential to generate glia steadily increased with neuronal output of the RGPs (Figure 3K), suggesting a correlation between neurogenic and gliogenic potential. Similar to SC neurogenesis, glial output by single RGPs was also highly variable (Figure 3L). Like neurons, clonally related glia were distributed throughout all layers regardless of clone induction time point (Figure 3M). The fraction of clones with glia in both colors decreased over time, suggesting a temporal progression of RGPs toward "asymmetric gliogenic" divisions (Figures 3N–3R). Finally, we compared the last neurogenic division in which the SC progenitor terminally divides to produce either two neurons (N+N clones) or one neuron and a glial progenitor committed to glial lineage (N+G clones). We observed that 14% of clones were N+G clones (Figure 3S), suggesting that ~1 in 7 neurogenic progenitors retained the capacity to generate glia, strikingly consistent with what was demonstrated in the cortex.[35] Taken together, our results revealed that gliogenesis occurs after neurogenesis from E12 onward. Similar to the cortex, the gliogenic capacity of RGPs correlates with neuronal output, although only a fraction of neurogenic RGPs produce glia.

MADM-CloneSeq reveals cell-type composition of individual clonal units

How do individual RGPs establish the full complement of neuronal diversity observed in mature SC? To address this issue, we conceived MADM-CloneSeq, an approach combining the power of MADM in generating individual high-confidence clonal units with scRNA-seq to determine the identity of clonally related cells (Figure 4A). Thus, MADM-CloneSeq enables unprecedented correlation of lineage relationship and cell-type identity while preserving precise spatial information of SC neurons *in situ*.

Using glass pipettes, we collected 399 neurons from 87 SC MADM clones induced at E10.5, using either *Fzd10*- or *Sox2*-CreER driver, from P28 acute brain slices. After Smart-seq2 RNA-seq, 253 cells from 58 clones passed quality filtering (Figures S6A–S6G; Table S1). We confirmed unbiased layer sampling of SC clones (chi-squared test; p = 0.322; Figure S6H). Our data analysis pipeline robustly assigned each MADM-CloneSeq cell to one of the 16 reference mature SC neuronal types,[24] including 6 excitatory and 10 inhibitory types (Figures 4B, S1E, and S1F). To verify precise cell-type assignment, we also showed that MADM-CloneSeq and reference cells shared highly similar marker gene expression when grouped into excitatory or inhibitory neuron types (Figure 4C), or individual subtypes (Figures S6I–S6J). Overall, we identified 117 excitatory and 136 inhibitory neurons (Figures 4D and S6K). While inhibitory neurons were most frequently sampled in the sSC, excitatory neurons showed an even distribution throughout the SC (chi-square goodness of fit: p = 5e−4 and p = 0.2, respectively; Figures 4E and S6L). Remarkably, all 16 neuronal cell types were detected among our MADM-CloneSeq cells, with SCEXC2 being overall the most abundant and SCINH4, 10, and 8 the least abundant neuronal types (Figures S6M and

(E–H) Representative reconstructions of SC MADM clones, induced at E9.5 (E), E10.5 (F), E11.5 (G), or E12.5 (H), and collected at P28. Each dot represents the location of a single red or green neuron. SC is outlined by a blue line, and layers are divided by blue dotted lines. Blue dot marks the location of the aqueduct (AQ).
(I and J) Quantification of clonal neuronal output in *MADM-11*$^{GT/TG}$*;Fzd10-CreER*$^{+/-}$ (*Fzd10*-clones) (I) and in *MADM-11*$^{GT/TG}$*;Sox2*$^{CreER/+}$ (*Sox2*-clones) (J). The number of neurons per clone (mean ± SEM) across induction time points plotted on the $\log_{10}$ scale. E9.5 (n = 33), E10.5 (n = 31), E11.5 (n = 32), and E12.5 (n = 30) in (I); E9.5 (n = 33), E10.5 (n = 39), E11.5 (n = 39), and E12.5 (n = 31) in (J). One-way ANOVA with Dunn's post-hoc test; p = 0.0113, p = 0.0358, and p = 0.0052 between consecutive time points in (I); p = 0.0192, p = 0.091, and p = 0.0476 between consecutive time points in (J); p = 0.7534, p > 0.9999, p > 0.9999, and p > 0.9999 of the same time point at E9.5, E10.5, E11.5, and E12.5 between (I) and (J), respectively. Red line, exponential one-phase decay curve fit of mean values.
(K) Quantification of the percentage of neurons (box, median with 25–75 percentiles; whiskers, 10–90 percentiles) located in each layer per clone across induction time points. Combined *Fzd10*- and *Sox2*-clones at E9.5 (n = 66), E10.5 (n = 70), E11.5 (n = 71), and E12.5 (n = 61). Two-way ANOVA; p < 0.0001 between sSC and dSC; p < 0.0001 between dSC and PAG; p = 0.9999, p = 0.9999, and p = 0.9999 between consecutive time points. **p < 0.01; ***p < 0.001.
(L–Q) Illustration and a representative clone for three categories of SC progenitor division patterns.
(R) Quantification of the proportion of all clones (mean with lower limits) in each category across induction time points; combined *Fzd10*- and *Sox2*-clones at E9.5 (n = 64), E10.5 (n = 68), E11.5 (n = 67), and E12.5 (n = 53). Fisher's exact test comparing proliferative and other clones; p = 0.000164, p = 0.034401, and p = 0.0000642 between consecutive time points. *p < 0.05; ***p < 0.001.
Scale bars, 200 μm (D–H, M, O, and Q).
See also Figures S2–S5.

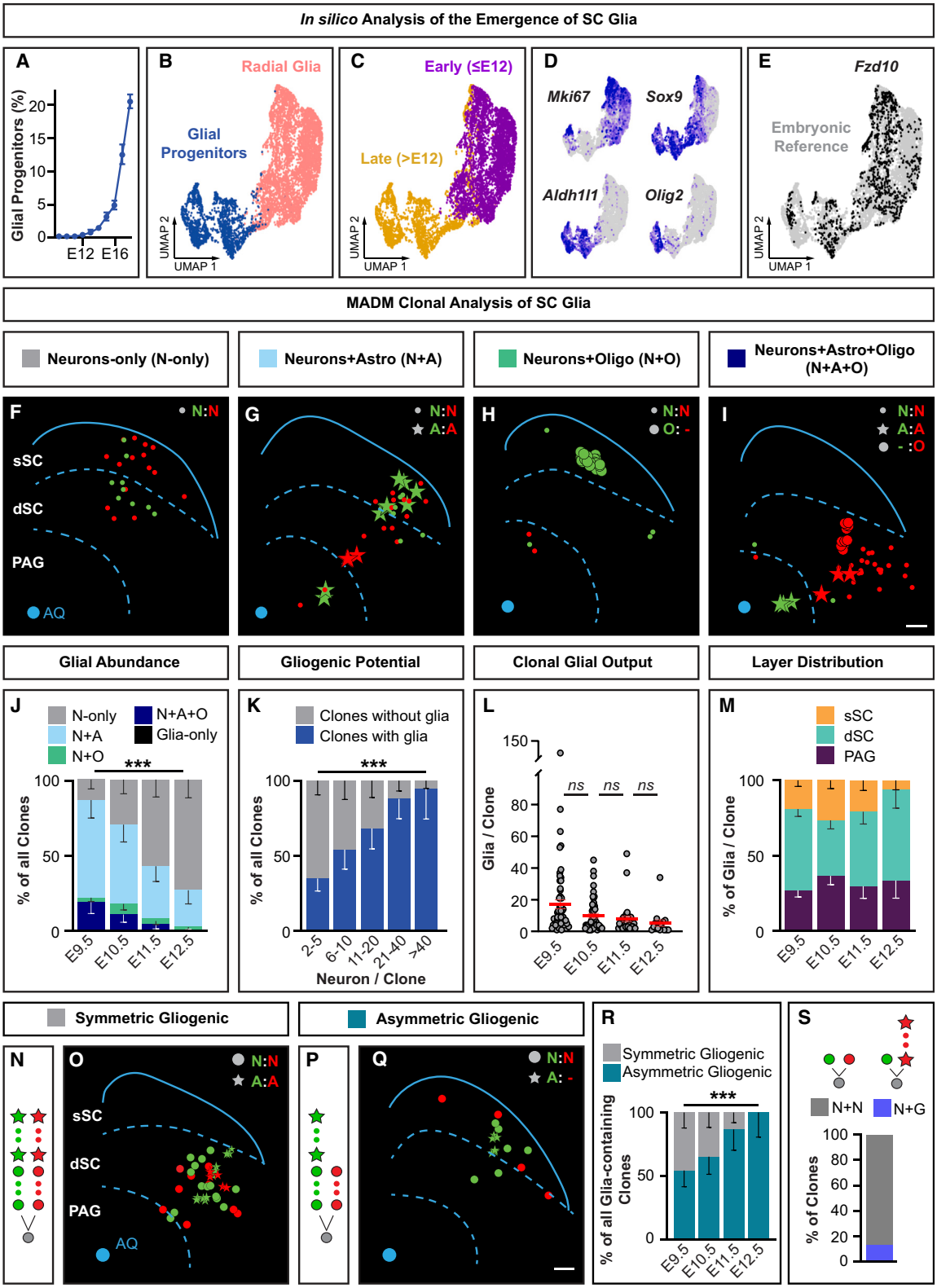

Figure 3. *In silico* and MADM clonal analysis of SC glia

(A) Line plot of relative abundance of glial progenitors in the dorsal midbrain based on embryonic reference dataset[23] (percentage ± 95% Clopper-Pearson confidence intervals).

(legend continued on next page)

S6N). Interestingly, 13 out of 16 neuronal types were preferentially located in distinct layers, with 7 in sSC, 3 in dSC, and 3 in PAG ($p < 0.1$, Z score; Figure S6O). Collectively, our MADM-CloneSeq data demonstrated that all known SC neuronal cell types were generated by resident RGPs.

Individual progenitors in SC are multipotent

Next, we exploited the power of MADM-CloneSeq to delineate the lineage relationships between different SC neuronal types by analyzing the neuron-type composition of individual clones. We obtained an average of 4 (ranging from 2 to 12) high-quality neurons in each clone (neurons per clone), which accounted for 60% (ranging from 31% to 100%) of all neurons per clone (Figures S7A and S7B). To examine the lineage relationship between excitatory vs. inhibitory neuron types, we first tested whether SC progenitors were restricted to producing one or the other type (Figures 4F and 4G). Remarkably, we found that 78% of clones were composed of both excitatory and inhibitory neuron types. Thus, we provide compelling evidence that glutamatergic excitatory and GABAergic inhibitory neurons originate from common progenitors in the developing SC (Figures 4H, 4I, and S7C). Clones consisting of only one type were significantly smaller ($p = 0.03$, t test) and included fewer cells sampled ($p = 0.002$, t test), suggesting that the probability of detecting both excitatory and inhibitory types likely depended on sample size (Figures S7D–S7F). To determine the potential of SC progenitors beyond "simple" excitatory and inhibitory properties, we analyzed the abundance of all 16 neuron types within individual clonal units (Figures 4J and 4K). We observed that the number of detected neuron types per clone increased with the number of cells per clone (Figure 4L; black dots), with no significant difference to the randomized dataset ($p_{adj} = 1$, Z score; Figure 4L; gray line and shaded area). Furthermore, nearly all possible pairs of neuron types were present within individual clones (98% of 120 possibilities; Figure 4M), with no pair showing significant preference of occurrence (Figure S7G). Our findings thus suggest that individual RGPs have the potential to generate the complete spectrum of neuronal cell types in the developing SC with no pre-defined cell-type linkage. The precise spatial location of sampled MADM-CloneSeq cells enabled us to assess lineage relationships between neuron types within and across SC layers. Using hierarchical clustering, we tested for any pattern of intra- or inter-laminar co-production of neuron types and found no significant preference (Figures S7H–S7O). Taken together, we demonstrated that SC RGPs are extraordinarily multipotent, with the capacity to produce the full spectrum of all neuron types, excitatory and inhibitory, without any pre-defined pattern related to location or their identity.

Multipotency is retained in individual terminally dividing SC progenitors

In order to truly comprehend the remarkable multipotency in SC progenitors and its impact on the generation of SC cell-type diversity, it was necessary to determine how multipotency might change as RGPs progress along their lineage. As both excitatory and inhibitory neurons emerged together in the developing midbrain at E12.5 (Figures 1D and 1E), it was not clear whether they may be produced by distinct lineage-specific progenitors at this stage. To address such issue, we examined terminally dividing RGPs, which were the majority of SC progenitors found at E12.5 in our MADM clonal analysis (Figure 2R). We assessed the potential of terminally dividing SC progenitors by asking whether the resulting "2-cell clones" contained exclusively excitatory or inhibitory, or a mixture of both neuron types (Figure 5A). We therefore performed MADM-CloneSeq on SC clones induced at E12.5 using either *Fzd10*- or *Sox2*-CreER driver and specifically sampled clones containing only two neurons to exclusively probe the products of terminal divisions (Figure 5A). We collected 36 neurons from 18 clones for RNA-seq and confirmed high RNA quality (Table S2). Using the same data analysis pipeline as described for MADM-CloneSeq of E10.5 clones, we assigned each cell to one of the reference SC neuronal types[24] and identified 15 excitatory and 21 inhibitory neurons (Figures 5B and 5C). Our analysis showed that 50% of our clones contained one excitatory and one inhibitory neuron,

(B and C) UMAPs showing distinct but connected clusters of radial glia and glial progenitors (B) and cells colored by real developmental origin extracted from embryos before (early) or after (late) E12.

(D) Expression of cell-type markers for dividing cells (*Mki67*), glial progenitors (*Sox9*), astrocytes (*Aldh1l1*), and oligodendrocytes (*Olig2*).

(E) UMAP showing *Fzd10*-lineage cells overlay with reference dataset.[23]

(F–I) Representative reconstructions of SC MADM clones, induced at E9.5, E10.5, E11.5, or E12.5, and collected at P28 in *MADM-11*$^{GT/TG}$*;Fzd10-CreER*$^{+/-}$ or *MADM-11*$^{GT/TG}$*;Sox2*$^{CreER/+}$ consisting of neurons only (N-only; F); neurons and astrocytes (N+A; G); neurons and oligodendrocytes (N+O; H); neurons, astrocytes, and oligodendrocytes (N+A+O; I). Each small dot represents the location of a single red or green neuron, stars for astrocytes, and larger dots for oligodendrocytes. SC is outlined by a blue line, and layers are divided by blue dotted lines. Blue dot marks the location of the aqueduct (AQ).

(J and K) Quantifications of the proportion of all clones (mean with lower limits) in each category of glial composition (J) and with or without glia (K) across induction time points; chi-square test, $p < 0.0001$ (J and K). Note that glia-only clones were never found.

(L and M) Quantifications of clonal glial output shown as the number of glia per clone (L; red lines, mean ± SEM) and percentage of glia located in each layer per clone (M; mean with SEM) across induction time points; one-way ANOVA with Dunn's post-hoc test; $p = 0.0689$, $p > 0.9999$, and $p = 0.3418$ between consecutive time points in (L). Two-way ANOVA; $p > 0.9999$ in (M).

(N–Q) Illustrations and representative clones for SC progenitor division patterns.

(R) Quantification of the proportion of all clones (mean with lower limits) in each category across induction time points; chi-square test, $p = 0.0005$.

(S) Illustrations and quantification of the relative proportions of clones producing one neuron in each subclone (N+N) or one neuron in one subclone but only glia in the other subclone (N+G).

Combined *Fzd10*- and *Sox2*-clones; n = 268 in (J) and (K); n = 152 glia-containing clones in (L), (M), and (R); n = 36 in (S).

Ns, not significant; ***$p < 0.001$.

Scale bars, 200 μm (F–I, O, and Q).

See also Figure S3.

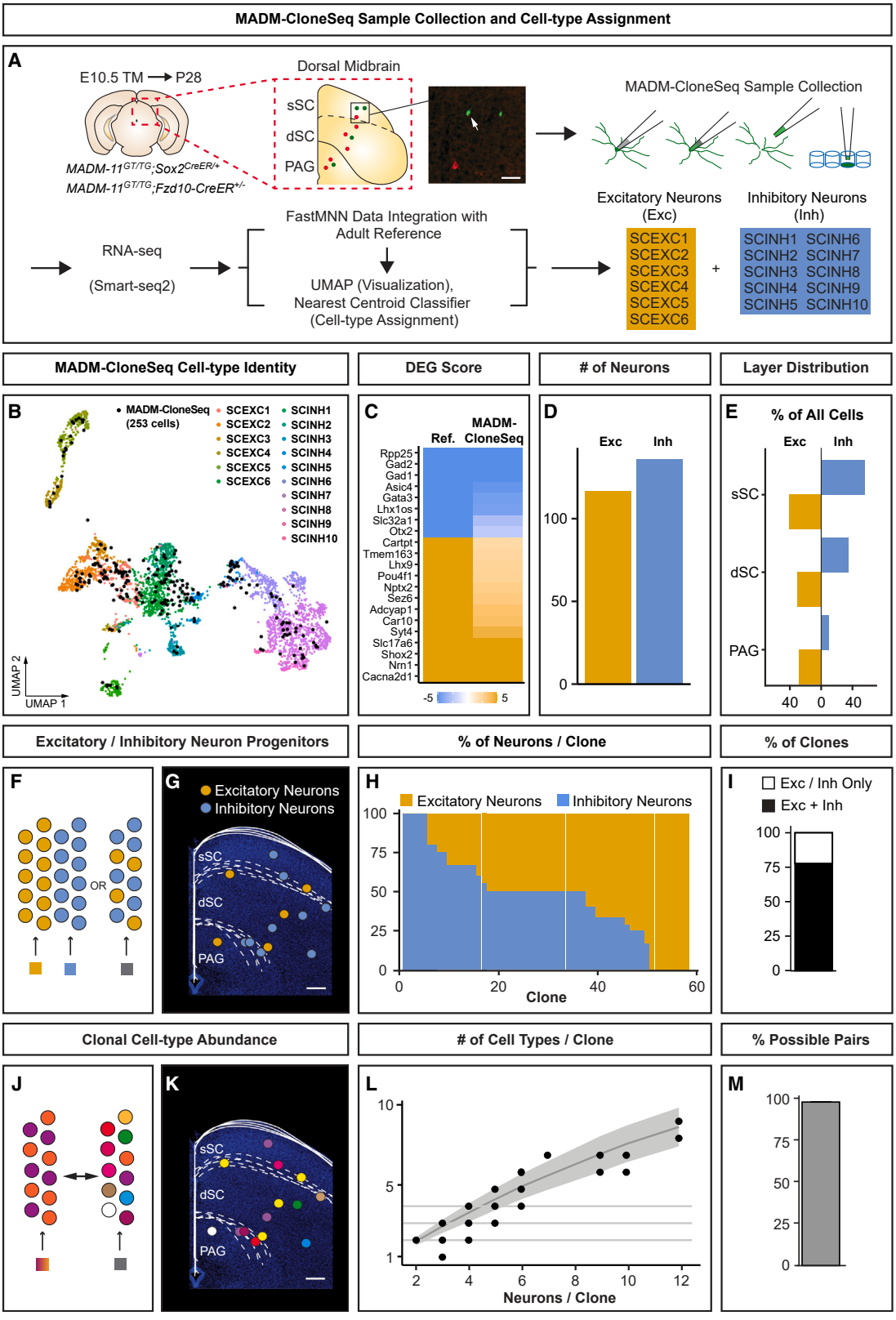

(legend on next page)

while 33% contained two inhibitory and 17% contained two excitatory neurons—not significantly different from a randomized dataset (Figures 5D and 5E). Furthermore, 15 out of 16 neuronal types were identified in our dataset (Figure 5F). Notably, the majority of clones (94%) contained two distinct neuronal types, strongly suggesting against any preference to co-produce the same types at the stage of terminal divisions (Figure 5G). Our findings thus provide unambiguous evidence that individual terminally dividing SC progenitors can generate both excitatory and inhibitory neurons and retain the capacity to produce all neuronal cell types. We therefore conclude that multipotency in individual SC progenitors persists until the last/terminal neurogenic division.

Pten is cell-autonomously required for establishing SC cell-type diversity

The multipotent nature of SC progenitors raises the key question of how defined proportions of different SC neuron types were established. To approach this issue, we turned to investigate the role of candidate signaling pathways. Specifically, we focused on Phosphatase and Tensin homolog gene (*Pten*), since loss of *Pten* in other brain areas (i.e., neocortex) has been shown to affect the ratios of specific interneuron types.[36] However, a possible cell-autonomous *Pten* function in SC ontogeny has not been assessed at the single-cell level. In the developing SC, *Pten* was expressed in RGPs throughout development, with the strongest expression level before E12 (Figure S8A), a time point at which SC neurons emerge (Figure 1C). We next utilized MADM technology and its exquisite single-cell labeling property to probe a putative cell-autonomous function of *Pten* in controlling SC neuronal cell-type abundance. We generated genetic mosaics where *Pten* was sparsely deleted in RGPs and compared the phenotype with wild-type RGPs in P0 and P28 SC (Figures 6A–6C and S8B). To this end, we recombined a *Pten*-flox allele onto chr19 containing the MADM reporter cassettes (see STAR Methods).[32,37] Next, we crossed *MADM-19*$^{TG/TG,Pten\text{-}flox}$ with *MADM-19*$^{GT/GT}$;*Nestin-Cre*$^{+/-}$ to generate *Pten*-MADM (*MADM-19*$^{GT/TG,Pten\text{-}flox}$;*Nestin-Cre*$^{+/-}$), with *Pten*$^{-/-}$ mutant cells labeled with GFP and *Pten*$^{+/+}$ control cells with tdT and control-MADM (*MADM-19*$^{GT/TG}$;*Nestin-Cre*$^{+/-}$; all cells *Pten*$^{+/+}$) (Figure S8C).

We first quantified the ratio of green to red cells in P0 and P28 SC and found a significant increase in *Pten*-MADM compared with control-MADM (Figures 6D–6M). Thus, the loss of *Pten* resulted in elevated overall SC neuron numbers, similar to observations in other brain areas.[38] However, whether the loss of *Pten* affects the number of specific SC neuron types was not clear. To resolve this issue, we isolated green *Pten*$^{+/+}$ and *Pten*$^{-/-}$ cells from the dorsal midbrain at P0 in control- and *Pten*-MADM mice, respectively, and subjected them to scRNA-seq using 10× Genomics technology (Figure 6N).

After quality filtering and data integration with reference dataset,[23] we retained 2,985 *Pten*$^{+/+}$ and 1,889 *Pten*$^{-/-}$ cells with dorsal midbrain annotation. For downstream analyses, we focused on 1,080 *Pten*$^{+/+}$ and 567 *Pten*$^{-/-}$ neuronal cells. Our dataset showed that while the relative distribution of immature and mature neurons was not altered by *Pten* deletion (Figures 6O and 6P), we detected more differentially expressed genes (DEGs) between *Pten*$^{+/+}$ and *Pten*$^{-/-}$ cells in immature than mature neurons (Figure 6Q). Gene Ontology (GO) enrichment analysis further revealed that *Pten*$^{-/-}$ immature neurons showed upregulation of terms related to cell cycle (Figures 6R and S8D), consistent with the reported role of *Pten* in cell proliferation.[39] *Pten*$^{-/-}$ mature neurons, on the other hand, were enriched in development- and interneuron-related GO terms (Figures 6R and S8E). The upregulation of interneuron-specific genes suggested a potential alteration of the overall SC neuronal cell-type composition upon deletion of *Pten*. To investigate this possibility, we focused on only mature neuronal populations (848 *Pten*$^{+/+}$ and 436 *Pten*$^{-/-}$ cells). UMAP and unsupervised clustering, together with marker expression analysis, identified excitatory-only, inhibitory-only, or mixed neuronal clusters (Figures 6S and S8F–S8H). The relative abundance of all three clusters was significantly altered upon *Pten* deletion, with a relative increase in inhibitory and a decrease in excitatory neuronal clusters (Figure 6T). To quantitatively assess whether all excitatory and inhibitory neuronal types were equally affected by *Pten* deletion, we

Figure 4. MADM-CloneSeq identifies multipotent progenitors with the capacity to generate all known SC neuronal types

(A) Workflow of MADM-CloneSeq using acute brain slices containing SC MADM clones (either *Fzd10*- or *Sox2*-clones), induced at E10.5 and collected at P28. Cells were assigned to one of 6 excitatory or 10 inhibitory neuronal types according to the reference dataset.[24]

(B) UMAP indicating the overlay of 253 MADM-CloneSeq cells (black dots) onto reference neurons (colored dots).

(C) Heatmap of DEG scores for selected genes expressed in excitatory (orange) and inhibitory (blue) neuronal types in reference and MADM-CloneSeq datasets.

(D and E) Quantification of the number of MADM-CloneSeq cells (D) and their relative layer distribution (E) for both excitatory (n = 117, orange) and inhibitory (n = 136, blue) neuronal types.

(F and G) Schematics illustrating two scenarios where individual SC progenitors either exclusively produce excitatory/inhibitory neuron types within a clonal unit or both neuron types (F). Hypothetical clone of the second scenario in (G).

(H) Bar plot showing the relative proportion of excitatory and inhibitory neurons sampled in each individual clone.

(I) Quantification of the overall proportion of clones (n = 58 combined *Fzd10*- and *Sox2*-clones) consisting of both excitatory and inhibitory neuron types (black) or just one type (white).

(J and K) Schematics illustrating two scenarios where individual SC progenitors generate either fixed or unrestricted clonal-cell-type composition (J). Hypothetical clone of the second scenario in (K).

(L) The number of distinct cell types identified in each clone is plotted over the number of neurons sampled per clone (n = 58 combined *Fzd10*- and *Sox2*-clones). Black line and gray ribbon indicate expected outcome for random cell-type choice for each cell within a clone. Distribution of MADM-CloneSeq data is not significantly different from randomized data at any clone size (*Z* score-associated p = 1 after multiple test correction).

(M) The percentage of observed cell-type pairs in any given clone relative to the total number of possible pairs, considering 16 neuronal types (n = 118 observed pairs/120 possibilities in combined *Fzd10*- and *Sox2*-clone).

Scale bars, 50 μm (A), and 200 μm (G and K).

See also Figures S6 and S7.

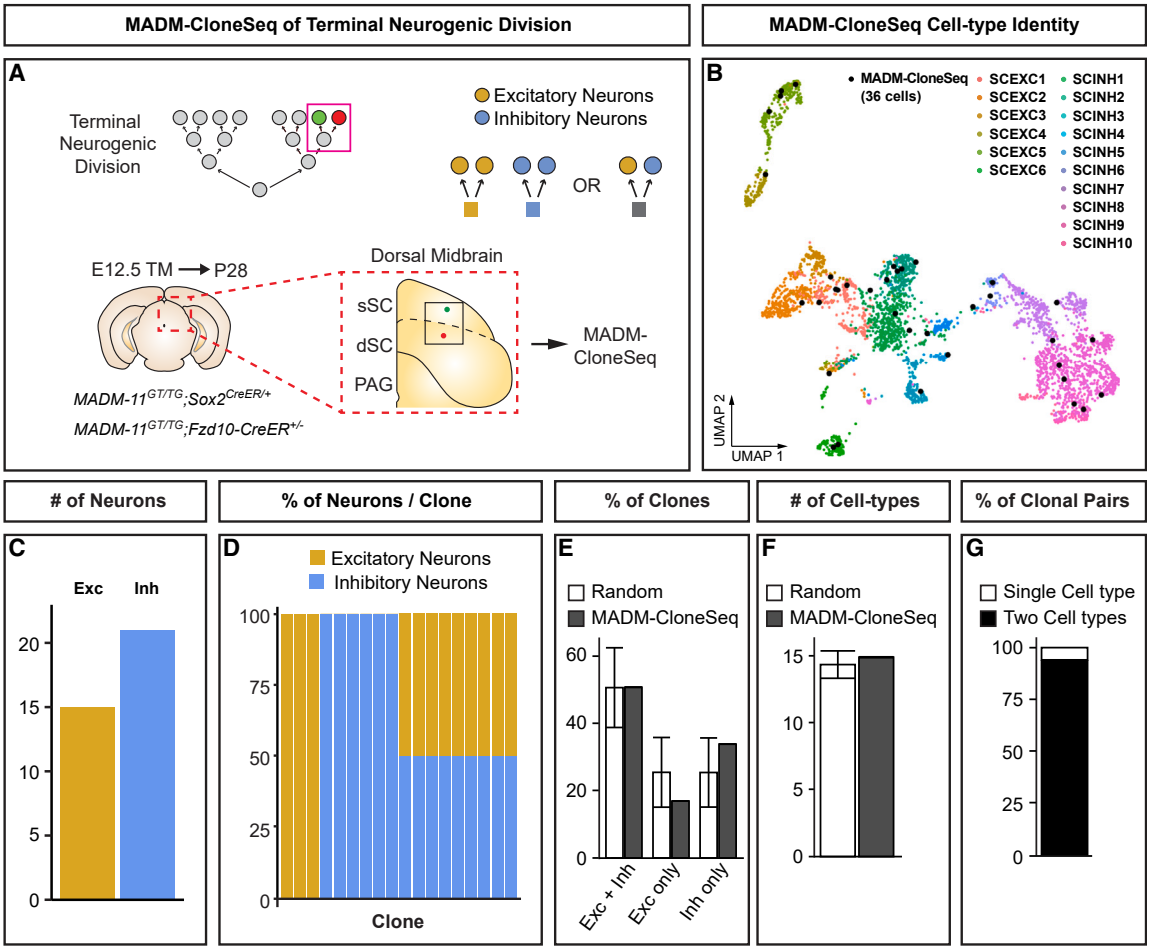

Figure 5. Individual terminally dividing SC progenitors are multipotent

(A) Schematics indicating MADM-labeled terminally dividing progenitor cell lineage (i.e., 2-cell MADM clone; top left), possible outcomes of cell-type combinations (top right), and MADM-CloneSeq strategy (bottom) using acute brain slices containing 2-cell MADM clones (either *Fzd10*- or *Sox2*-clones), induced at E12.5 and collected at P28.

(B) UMAP indicating the overlay of 36 MADM-CloneSeq cells (black dots) onto reference neurons (colored dots). Cells were assigned to one of 6 excitatory or 10 inhibitory neuronal types according to the reference dataset.[24]

(C) Quantification of the number of MADM-CloneSeq cells for excitatory (n = 15) and inhibitory (n = 21) neuronal types.

(D) Bar plot showing the relative proportion of excitatory and inhibitory neurons sampled in each individual 2-cell MADM clone.

(E) Proportions of clones with different combinations of excitatory (Exc) and inhibitory (Inh) neurons compared with randomized data (chi-squared, p = 0.6065).

(F) Number of distinct neuronal cell types identified in MADM-CloneSeq data compared with randomized data (*Z* score, p = 0.591).

(G) Quantification of the overall proportion of clones consisting of two different cell types (black) or only one cell type (white).

Bars and error bars depict mean and standard deviation of randomized data in (E) and (F).

assigned cluster labels from Figure S1C to each neuron and compared the relative abundance of individual clusters between control and *Pten* knockout (KO). We found that *Pten* deletion significantly altered the relative abundance of specific neuronal clusters (2, 3, 7, 8, and 9), while the rest (clusters 1, 4, 5, and 10) remained unchanged (Figures 6U and 6V). Among the affected clusters, the largest excitatory cluster (2) was decreased, whereas the largest inhibitory cluster (3) was increased upon *Pten* deletion. By superimposing velocities of developmental trajectories onto the neuronal cluster UMAP (Figure 6U), we revealed that the imbalance of excitatory and inhibitory abundance upon *Pten* deletion followed a trajectory-specific pattern. In the absence of *Pten* function, inhibitory neuron clusters 3 and 9, which appeared to originate from a distinct trajectory, became more abundant at the expense of neuron clusters 2, 7, and 8. We next investigated whether the effect of *Pten* deletion may differentially affect the abundance of specific adult GABAergic neuronal subtypes. Our previous analysis demonstrated that clusters 3 and 9 shared high levels of similarities with specific adult GABAergic types SCINH1, SCINH2, SCINH3, SCINH6, and SCINH10 (Figure 1H). We extracted inhibitory neurons from the adult reference dataset[24] and visualized the expression of markers of several well-known SC inhibitory neuron types.[40] Our analysis revealed that SCINH1 and SCINH3 were a subset of parvalbumin (PV)-positive neurons, SCINH2 and

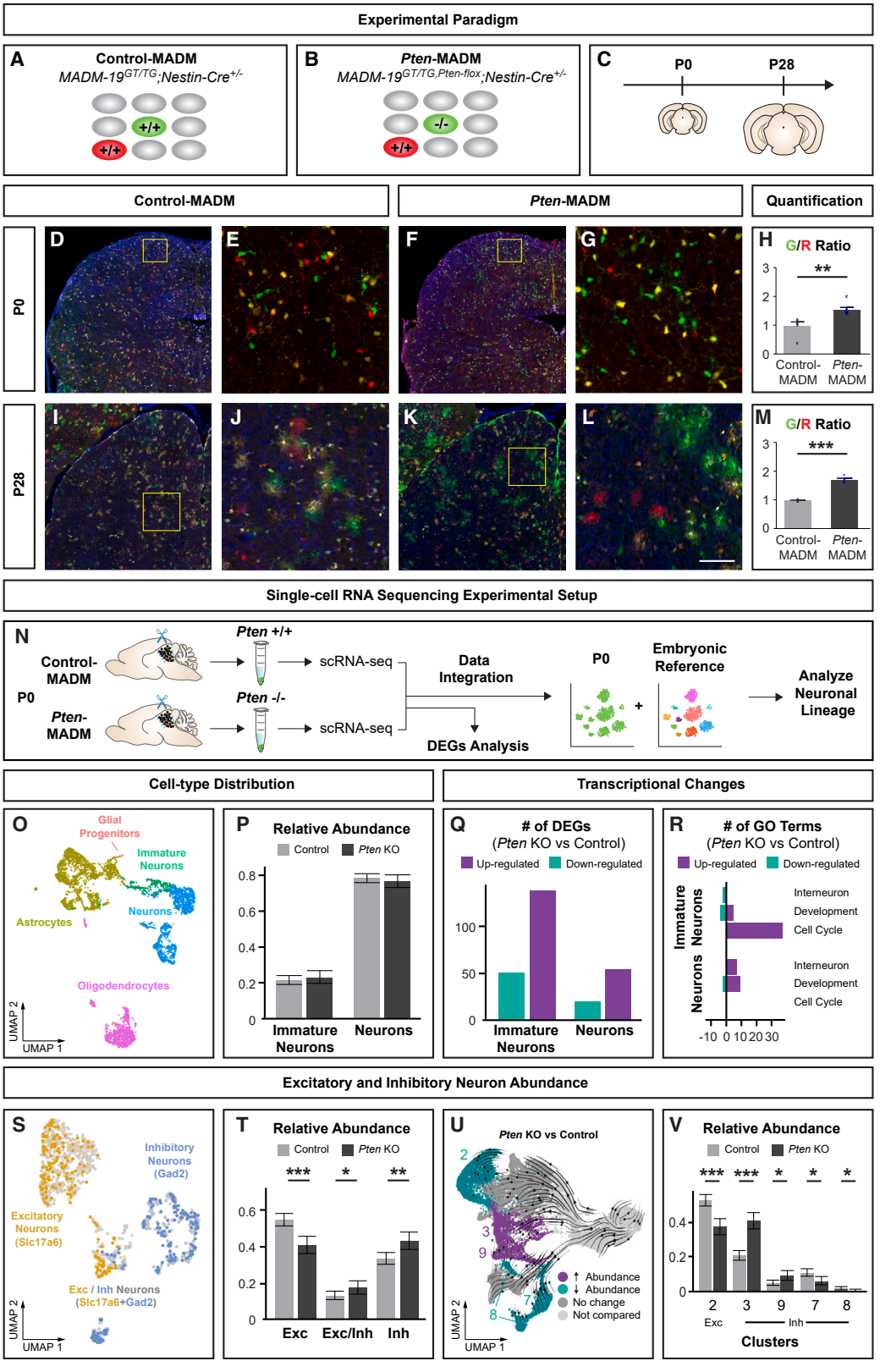

(legend on next page)

SCINH10 were a subset of calbindin 2 (CB)-positive neurons, and SCINH6 represented the only cluster of somatostatin (SST)-positive neurons (Figures S8I and S8J). Thus, we predict that *Pten* deletion may selectively increase the relative abundance of specific molecularly defined GABAergic neuronal types with potential functional impact. Altogether, our results revealed an essential cell-autonomous *Pten* function in establishing an appropriate quantitative balance of distinct excitatory and inhibitory neuron types and thus overall neuronal SC cell-type diversity.

DISCUSSION

In the developing SC, RGPs establish the full spectrum of cell-type diversity. However, the underlying fundamentals regulating RGP proliferation behavior, neurogenic and gliogenic potential, and lineage progression are poorly understood. In our study, we capitalized upon the exquisite single-cell resolution of the MADM approach, in combination with scRNA-seq technologies, to pursue systematic cell lineage tracing in SC *in silico* and *in situ*, preserving the complete spatial information. We found a common pool of resident progenitors that can generate the full spectrum of all known neuronal types to occupy the distinct layers in the mature SC. Individual RGPs progress rapidly from proliferative to neurogenic and then to gliogenic proliferation mode and show exceptional multipotency from early stages in their lineage until their terminal neurogenic division. Collectively, our results define the cellular principles and provide an inaugural ontogenetic framework of the SC at single-RGP/-cell level (Figure 7). We discuss our findings in the general context of neural stem cell lineage progression and RGP multipotency in the generation of neuronal cell-type diversity.

RGP lineage progression in developing SC

The SC constitutes a laminar structure similar to the cerebral cortex where the consecutive buildup of distinct layers follows a precise temporally stereotyped pattern.[41,42] For instance, earlier-born corticofugal cortical projection neurons occupy lower layers, and later-born callosal neurons locate primarily to the upper layers.[43,44] Interestingly, using 3^{H}-thymidine autoradiography and analysis at the population level, previous studies indicated possible inside-out order of SC lamina emergence.[45] However, our spatiotemporal analysis of individual MADM clones with single-cell resolution did not indicate any temporally stereotyped pattern of SC lamina appearance. Instead, SC neurons born at earlier stages did not exclusively populate the PAG and/or dSC, and later-born neurons were distributed across the PAG and both sSC and dSC laminae. Thus, temporal RGP lineage progression could not predict the laminar position of nascent SC neurons, unlike in the developing neocortex. Recent work[46] (https://neurobirth.org/) using advanced birth-dating methods to catalog neurogenesis in different brain regions including SC provided findings at a population level consistent with ours. The authors found that the peak of SC neurogenesis was earlier and much quicker than it was during corticogenesis (~E11–E13). They also observed that neurogenesis of distinct SC layers was much less temporally defined than that of the cortical layers. Importantly, SC neurons did not appear to follow a temporal order of production, i.e., displayed a lack of inside-out order of generation.

The progression of neocortical RGP lineage follows a highly stereotyped temporal sequential pattern, and the neuronal output at any given stage is highly predictable. Once neocortical RGPs switch from proliferative division mode to asymmetric neurogenic mode at a critical time, RGPs produce ~8–9 postmitotic neurons.[35] In stark contrast, there is no clear temporal separation of proliferative and neurogenic division modes in the developing SC. Furthermore, the neurogenic output of individual SC RGPs is highly variable throughout the neurogenic window, albeit the overall output decreases exponentially from E9.5 to E12.5, contrasting the unitary output of neurogenic neocortical

Figure. 6. *Pten* is required for appropriate relative proportions of SC excitatory/inhibitory neuron types

(A–C) Experimental mosaic MADM paradigms to assess cell-autonomous *Pten* function in establishing SC cell-type diversity. In control-MADM (*MADM-19*$^{GT/TG}$; *Nestin-Cre*$^{+/-}$) (A), all cells were *Pten*$^{+/+}$, whereas in mosaic *Pten*-MADM (*MADM-19*$^{GT/TG,Pten\text{-}flox}$;*Nestin-Cre*$^{+/-}$) (B), red cells were *Pten*$^{+/+}$ and green cells *Pten*$^{-/-}$. Sparse MADM labeling enables us to probe the cell-autonomous function with single-cell resolution in time course at P0 and P28 (C). See also Figures S8B and S8C.

(D–M) Representative images (D–G and I–L) and quantification (H and M) of MADM-labeled cells in SC at P0 (D–H) and P28 (I–M) in control-MADM (D, E, I, and J) and *Pten*-MADM (F, G, K, and L). Magnified images of yellow boxed regions are shown in (E), (G), (J), and (L). Quantification of green/red ratio (mean ± SEM) of cells at P0 (H) and neurons at P28 (M) in control-MADM: n = 5 in (H) and 4 in (M); *Pten*-MADM: n = 7 in (H) and 4 in (M). Mann-Whitney test, p = 0.0025 in (H); t test; p = 0.00002 in (M). **p < 0.01; ***p < 0.001.

(N) Experimental setup to isolate MADM-labeled green cells in control-MADM (*Pten*$^{+/+}$) and in *Pten*-MADM (*Pten*$^{-/-}$) at P0 in dorsal midbrain for scRNA-seq and data analysis. Data integration was performed using the reference dataset.[23]

(O) UMAP indicating distinct clusters of neuronal and glial cell types in dorsal midbrain at P0 and identified based on reference annotations (n = 2,985 *Pten*$^{+/+}$ and n = 1,889 *Pten*$^{-/-}$ cells).

(P) Relative abundance (fraction ± 95% Clopper-Pearson confidence intervals) of immature and mature control (light gray, n = 1,080) and *Pten* KO (dark gray, n = 567) neurons; chi-squared p = 0.49.

(Q and R) Number of up- or down-regulated DEGs (Q) and their associated GO terms (R) in *Pten* KO compared with control were plotted for immature and mature neurons. GO terms for interneuron, developmental, and cell cycle categories were indicated.

(S) UMAP clusters containing either excitatory-only, inhibitory-only, or mixed neuronal populations of n = 848 *Pten*$^{+/+}$ and n = 436 *Pten*$^{-/-}$ cells.

(T) Relative abundance (fraction ± 95% Clopper-Pearson confidence intervals) of each type was indicated between control (light gray) and *Pten* KO (dark gray). Chi-squared statistics per category after multiple test correction; p = 9.9 × 10^{-6} for Exc, p = 0.048 for Exc/Inh, and p = 0.0013 for Inh.

(U and V) Cluster (as identified in Figure S1C) assignment of control and *Pten* KO cells and relative abundance of control (light gray) and *Pten* KO (dark gray) cells in each cluster. Significant changes are highlighted on UMAP as higher/lower/unchanged in *Pten* KO relative to control (U) and indicated as relative distribution (fraction ± 95% Clopper-Pearson confidence intervals) in bar plot (V). Chi-squared statistics per cluster after multiple test correction; 9.5× 10^{-7} for cluster 2; 4.4 × 10^{-13} for cluster 3; 0.014 for cluster 9; 0.014 for cluster 7; and 0.09 for cluster 8. *p < 0.1; **p < 0.01; ***p < 0.001.

Scale bars, 200 μm (D and F), 30 μm (E–G), 400 μm (I–K), and 90 μm (J and L).

See also Figure S8.

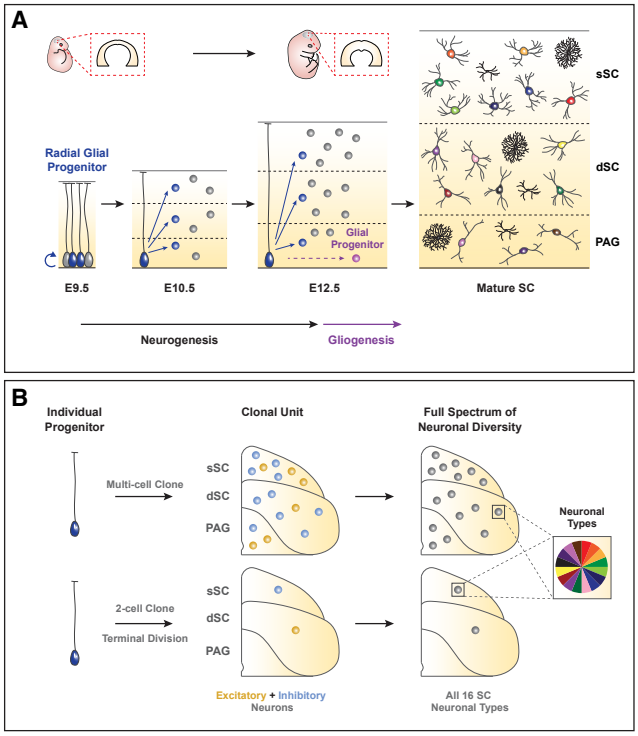

Figure 7. Multipotent progenitors instruct ontogeny and the generation of cell-type diversity in developing SC

(A) Framework of SC ontogeny. During early SC development at E9.5, the vast majority of radial glial progenitors (RGPs) self-amplify through proliferative cell divisions to increase their progenitor pool. Thereafter, between E10.5 and E12.5, RGPs undergo neurogenic divisions to produce nascent neurons destined for all layers (sSC, superficial SC; dSC, deep SC; PAG, periaqueductal gray), regardless of developmental time. SC gliogenesis occurs after neurogenesis in a subset of RGPs. In their rapid lineage progression, multipotent resident RGPs ultimately produce the full complement of all neuronal cell types as well as astrocytes and oligodendrocytes as observed in the mature SC.

(B) Generation of neuronal cell-type diversity in developing SC. During their entire neurogenic phase, individual progenitors exhibit full multipotent potential regardless of the size of their neuronal output (clonal unit). Regardless, if individual RGPs produce many clonally related cells (multi-cell clone) or only two cells in a terminal division (2-cell clone), RGPs can generate both excitatory and inhibitory neurons at near-random frequency. At the level of all neuronal types (based on single-cell transcriptome), each RGP retains full multipotency with the capacity to generate the complete spectrum of all 16 SC neuron types (represented by the inset of a cell with 16 colors), without any predefined composition or preference.

RGPs. SC gliogenesis, however, seems largely analogous to neocortical glia production. MADM glial clonal analysis revealed that neurogenesis strictly precedes glia production, beginning ~E12.5, and that only a fraction of neurogenic RGPs continued to produce glia.[35,47] Nevertheless, SC progenitors clearly progress in a less predictable manner in their lineage than neocortical RGPs. Interestingly, neurogenesis in the developing retina appears to occur in even more unpredictable pattern[48,49] where progenitors are thought to be subjected to stochastic factors during lineage progression.[50,51] However, unlike in the developing SC, retinal cell types are produced over a prolonged period of embryonic and postnatal neurogenesis lasting until P11.[52,53] Thus, despite less predictable lineage pattern, SC RGPs complete neurogenesis rapidly during embryogenesis (in just about 3 days), thereby limiting the available developmental time window and thus lineage-influencing factors.

Emergence of cell-type diversity in SC

Ever since the identification of RGPs in the mouse SC[4] and optic tectum in non-mammalian vertebrates,[16,17] their neurogenic potential has not been determined at the individual progenitor level. Whether resident RGPs constitute the sole source of SC neuron types is also not clear. In effect, in many brain areas, excitatory and inhibitory neuron types emerge from genetically distinct RGP types, and their generation is spatially and/or temporally segregated. For instance, glutamatergic excitatory projection neurons in the developing neocortex emerge from RGPs located in the ventricular zone of the dorsal telencephalon,[44,54–56] whereas GABAergic cortical inhibitory neurons originate from RGPs in the ventral ganglionic eminences.[57–59] Likewise, distinct neuron types destined for the olfactory bulb,[60,61] ventral midbrain,[62] or the cerebellum[63] are generated at very distant "tissue-extrinsic" progenitor niches. In the developing SC, however, our systematic *in silico* and *in situ* cell lineage tracing revealed that all neuron types, including the full spectrum of glutamatergic excitatory and GABAergic inhibitory neurons, emerge from local RGPs. At least at the qualitative level based on transcriptional signature, no extrinsic source was required to establish the complete set of SC neuronal types. It will be interesting to assess in the future whether and how putative SC-external sources could add quantitatively to the overall cell numbers.

At the molecular level, the MADM-based analysis identified a cell-autonomous role of *Pten* in establishing appropriate relative SC neuron-type abundance. Interestingly, previous work has shown that deletion of *Pten* was associated with enlarged midbrain structures, which in turn disrupted sensory processing in mice.[64,65] Furthermore, conditional ablation of *Pten* in cortical interneurons resulted in a cell-type-specific increase of PV/SST neuron ratio.[36] However, a general role for PTEN signaling in generating overarching cell-type diversity in a particular brain region has not been defined. In our study, we showed that *Pten* deletion results in an overall increase of $Pten^{-/-}$ mutant cells in SC. However, the relative fractions of certain SC excitatory neuron types were significantly decreased, whereas particular inhibitory neuron types were increased. The bias in SC neuron types, likely including specific subsets of PV-, SST-, and CB-expressing inhibitory neurons, appeared to emerge in a developmental trajectory-specific manner, implying critical *Pten* function at specific inferred cell lineage points during SC development. It will thus be important in the future to isolate molecular correlates that define these critical lineage points. In conclusion, *Pten* function seems not only necessary for appropriate relative excitatory/inhibitory neuron-type numbers but more generally for the faithful establishment of overall cell-type diversity in the developing SC.

RGP multipotency and lineage relationship in generating neuronal diversity in SC

How RGP lineage and thus clonal relationship contribute to the generation of cell-type diversity in the developing brain is a

fundamental issue but incompletely understood. In order to obtain definitive information, it is essential to trace RGP-derived lineages at the single-cell level and determine the cell identity of all sibling cells *in situ*. The MADM-CloneSeq approach that we have presented here provides a genetic approach combining *in vivo* cell lineage information and transcriptional cell-type identity with preserved spatial information. By using MADM-CloneSeq, we have demonstrated in our study that individual SC RGPs can generate the complete spectrum of all excitatory and inhibitory neuron types. Individual RGP MADM clones in mature SC did not show any pre-defined cell-type composition, even in two-cell clones originating from terminal RGP division. Hence, RGPs in the developing SC show multipotency along their entire neurogenic lineage.

A seemingly shared common lineage of excitatory and inhibitory neurons has been reported in progenitors located within the p2 domain in the developing spinal cord and generating both v2aINs (excitatory) and v2bINs (inhibitory) neurons[66] although these data emerged from population analysis rather than single-clone assessment. Thus, whether p2 progenitors, at the individual progenitor level, are truly bi-potent (and to which extent along their lineage) remains to be clarified. Perhaps interestingly, recent MADM-based clonal analysis revealed a nested smaller (<20%) population of embryonic *Sox2*$^+$ progenitors with the potential to generate two specific neuronal types in the cerebellum, namely, GABAergic Purkinje cells (PCs) and glutamatergic granule cells (GCs).[67] However, the generation of cerebellar inhibitory PCs and excitatory GCs is strictly separated in large spatiotemporal dimensions. While PCs are generated around E12 by progenitors residing in the embryonic ventricular zone, GCs are only produced several weeks later at postnatal stages when progenitors locate to the external granule cell layer.[68] Thus, the prolonged temporal period correlating with this nested population of bi-potent cerebellar progenitors, in combination with changing extrinsic signaling cues, may likely explain their neurogenic potency. Whether truly multipotent cerebellar progenitors, with the capacity to produce all the distinct cerebellar neuron types, exist, awaits further investigation. By contrast, >75% of SC progenitors showed multipotency and even beyond "simple" classification of excitatory and inhibitory neuron fate. Regardless of the precise molecular mechanisms that regulate SC multipotent progenitor fate potential, it is intriguing to note that in both spinal cord and cerebellar progenitor niches, Notch signaling appears to instruct the binary cell fate choice.[66,67]

Cardinal multipotent progenitors, generating the major cell types, have been described in the retina.[69–72] However, similar to cerebellum, different retinal cell types are generated during prolonged periods including from embryonic[49] to postnatal[48] developmental stages. By contrast, the production of all distinct neuron types in SC occurs within a narrow (2–3 days) developmental time window. To corroborate our data, a recent study using bromodeoxyuridine (BrdU) labeling methods and immunohistochemistry showed that nascent SC neurons born at E12.5 were already immunopositive for either excitatory or inhibitory markers 16 h later.[14] Thus, the multipotency of SC RGPs appears to precipitate in very short developmental period. The extent of RGP multipotency in SC lasts up to the terminal progenitor cell division based on our two-cell MADM clone dataset. Hence, SC RGPs at their final division can still produce any pair of distinct neuronal types. By contrast, retinal progenitors appear to lose or restrict some of their multipotency over time because progenitors isolated postnatally produced only four different retinal cell types.[48] Furthermore, several studies have identified terminally dividing retinal progenitors that showed certain bias in the fate potential of their two daughter cells.[73–75]

In conclusion, bi-/multipotent progenitors have been identified in certain developing stem cell niches besides SC. However, whether they all show true multipotency at the individual progenitor level, and if they retain full multipotency along the entire lineage, is not clear. While in certain lineages, e.g., the developing retina, progenitor fate-restriction over time seems evident, RGPs in SC preserved their full multipotency until the last neurogenic division. Importantly, the neurogenic period in multipotent SC RGPs was very short, lasting just a few days, while progenitors in the retina (and to some extent cerebellum) produce the full spectrum of distinct cell types over the course of several weeks. Taken together, our data provide an inaugural ontogenetic framework of SC development at single-cell resolution and revealed the cellular principles of SC RGP lineage progression in establishing neuronal cell-type diversity.

STAR★METHODS

Detailed methods are provided in the online version of this paper and include the following:

- KEY RESOURCES TABLE
- RESOURCE AVAILABILITY
  - Lead contact
  - Materials availability
  - Data and code availability
- EXPERIMENTAL MODEL AND SUBJECT DETAILS
  - Mice
- METHOD DETAILS
  - Generation of Experimental Mice
  - Single-cell RNA Sequencing
  - Collection of MADM-labeled Tissue for Histological Studies
  - MADM-CloneSeq
- QUANTIFICATION AND STATISTICAL ANALYSIS
  - MADM Clonal Analysis and 3D Reconstruction of Clones
  - RNA Sequencing Data Analysis
  - Statistical analysis

SUPPLEMENTAL INFORMATION

Supplemental information can be found online at https://doi.org/10.1016/j.neuron.2023.11.009.

ACKNOWLEDGMENTS

We thank Liqun Luo for his continued support, for providing essential resources for generating *Fzd10*-CreER mice that were generated in his laboratory, and for comments on the manuscript; W. Zhong for providing *Nestin*-Cre transgenic mouse line for this study; A. Heger for mouse colony management; R. Beattie and T. Asenov for designing and producing components of acute slice recovery chamber for MADM-CloneSeq experiments; and K.

Leopold, J. Rodarte, N. Amberg, and R. Bondarenko for initial experiments, technical support, and/or assistance. This study was supported by the Scientific Service Units of IST Austria through resources provided by the Imaging & Optics Facility, Laboratory Support Facility, Miba Machine Shop, and Preclinical Facility. G.C. received funding from the European Commission (IST plus postdoctoral fellowship). This work was supported by ISTA institutional funds, the Austrian Science Fund Special Research Programmes (FWF SFB-F78 Neuro Stem Modulation), to S.H.

AUTHOR CONTRIBUTIONS

G.C., F.M.P., and S.H. conceived the research. G.C., F.M.P., and S.H. designed all experiments and interpreted the data. G.C., F.M.P., P.K., T.K., C.S., M.S., N.G.-O., and A.E.I. performed all the experiments. S.H., C.B., and R.S. provided reagents and/or resources. S.H. supervised the project. G.C., F.M.P., and S.H. wrote the manuscript. All authors edited and proofread the manuscript.

DECLARATION OF INTERESTS

C.B. is a cofounder and scientific advisor of Myllia Biotechnology and Neurolentech.

INCLUSION AND DIVERSITY

We support inclusive, diverse, and equitable conduct of research.

Received: July 29, 2023
Revised: October 6, 2023
Accepted: November 10, 2023
Published: December 13, 2023

REFERENCES

1. Cang, J., Savier, E., Barchini, J., and Liu, X. (2018). Visual function, organization, and development of the mouse superior colliculus. Annu. Rev. Vis. Sci. *4*, 239–262.
2. Basso, M.A., Bickford, M.E., and Cang, J. (2021). Unraveling circuits of visual perception and cognition through the superior colliculus. Neuron *109*, 918–937.
3. Oliveira, A.F., and Yonehara, K. (2018). The mouse superior colliculus as a model system for investigating cell type-based mechanisms of visual motor transformation. Front. Neural Circuits *12*, 59.
4. Edwards, M.A., Caviness, V.S., Jr., and Schneider, G.E. (1986). Development of cell and fiber lamination in the mouse superior colliculus. J. Comp. Neurol. *248*, 395–409.
5. May, P.J. (2006). The mammalian superior colliculus: laminar structure and connections. Prog. Brain Res. *151*, 321–378.
6. Seabrook, T.A., Burbridge, T.J., Crair, M.C., and Huberman, A.D. (2017). Architecture, function, and assembly of the mouse visual system. Annu. Rev. Neurosci. *40*, 499–538.
7. Ito, S., and Feldheim, D.A. (2018). The mouse superior colliculus: an emerging model for studying circuit formation and function. Front. Neural Circuits *12*, 10.
8. Sanes, J.R., and Zipursky, S.L. (2020). Synaptic specificity, recognition molecules, and assembly of neural circuits. Cell *181*, 536–556.
9. Benavidez, N.L., Bienkowski, M.S., Zhu, M., Garcia, L.H., Fayzullina, M., Gao, L., Bowman, I., Gou, L., Khanjani, N., Cotter, K.R., et al. (2021). Organization of the inputs and outputs of the mouse superior colliculus. Nat. Commun. *12*, 4004.
10. Guillamón-Vivancos, T., Aníbal-Martínez, M., Puche-Aroca, L., Moreno-Bravo, J.A., Valdeolmillos, M., Martini, F.J., and López-Bendito, G. (2022). Input-dependent segregation of visual and somatosensory circuits in the mouse superior colliculus. Science *377*, 845–850.
11. Jure, R. (2018). Autism pathogenesis: the superior colliculus. Front. Neurosci. *12*, 1029.
12. McFadyen, J., Dolan, R.J., and Garrido, M.I. (2020). The influence of subcortical shortcuts on disordered sensory and cognitive processing. Nat. Rev. Neurosci. *21*, 264–276.
13. Tan, S.S., Valcanis, H., Kalloniatis, M., and Harvey, A. (2002). Cellular dispersion patterns and phenotypes in the developing mouse superior colliculus. Dev. Biol. *241*, 117–131.
14. Arimura, N., Dewa, K.I., Okada, M., Yanagawa, Y., Taya, S.I., and Hoshino, M. (2019). Comprehensive and cell-type-based characterization of the dorsal midbrain during development. Genes Cells *24*, 41–59.
15. Achim, K., Salminen, M., and Partanen, J. (2014). Mechanisms regulating GABAergic neuron development. Cell. Mol. Life Sci. *71*, 1395–1415.
16. Gray, G.E., and Sanes, J.R. (1992). Lineage of radial glia in the chicken optic tectum. Development *114*, 271–283.
17. Vanselow, J., Thanos, S., Godement, P., Henke-Fahle, S., and Bonhoeffer, F. (1989). Spatial arrangement of radial glia and ingrowing retinal axons in the chick optic tectum during development. Brain Res. Dev. Brain Res. *45*, 15–27.
18. Gale, S.D., and Murphy, G.J. (2014). Distinct representation and distribution of visual information by specific cell types in mouse superficial superior colliculus. J. Neurosci. *34*, 13458–13471.
19. Masullo, L., Mariotti, L., Alexandre, N., Freire-Pritchett, P., Boulanger, J., and Tripodi, M. (2019). Genetically defined functional modules for spatial orienting in the mouse superior colliculus. Curr. Biol. *29*, 2892–2904.e8.
20. Shang, C., Liu, Z., Chen, Z., Shi, Y., Wang, Q., Liu, S., Li, D., and Cao, P. (2015). Brain circuits. A parvalbumin-positive excitatory visual pathway to trigger fear responses in mice. Science *348*, 1472–1477.
21. Villalobos, C.A., Wu, Q., Lee, P.H., May, P.J., and Basso, M.A. (2018). Parvalbumin and GABA microcircuits in the mouse superior colliculus. Front. Neural Circuits *12*, 35.
22. Li, Y.T., and Meister, M. (2023). Functional cell types in the mouse superior colliculus. eLife *12*.
23. La Manno, G., Siletti, K., Furlan, A., Gyllborg, D., Vinsland, E., Mossi Albiach, A., Mattsson Langseth, C., Khven, I., Lederer, A.R., Dratva, L.M., et al. (2021). Molecular architecture of the developing mouse brain. Nature *596*, 92–96.
24. Zeisel, A., Hochgerner, H., Lönnerberg, P., Johnsson, A., Memic, F., van der Zwan, J., Häring, M., Braun, E., Borm, L.E., La Manno, G., et al. (2018). Molecular architecture of the mouse nervous system. Cell *174*, 999–1014.e22.
25. Xie, Z., Wang, M., Liu, Z., Shang, C., Zhang, C., Sun, L., Gu, H., Ran, G., Pei, Q., Ma, Q., et al. (2021). Transcriptomic encoding of sensorimotor transformation in the midbrain. eLife *10*.
26. Liu, Y., Savier, E.L., DePiero, V.J., Chen, C., Schwalbe, D.C., Abraham-Fan, R.J., Chen, H., Campbell, J.N., and Cang, J. (2023). Mapping visual functions onto molecular cell types in the mouse superior colliculus. Neuron *111*, 1876–1886.e5.
27. Choi, J.S., Ayupe, A.C., Beckedorff, F., Catanuto, P., McCartan, R., Levay, K., and Park, K.K. (2023). Single-nucleus RNA sequencing of developing superior colliculus identifies neuronal diversity and candidate mediators of circuit assembly. Cell Rep. *42*, 113037.
28. Muzumdar, M.D., Tasic, B., Miyamichi, K., Li, L., and Luo, L. (2007). A global double-fluorescent Cre reporter mouse. Genesis *45*, 593–605.
29. Zong, H., Espinosa, J.S., Su, H.H., Muzumdar, M.D., and Luo, L. (2005). Mosaic analysis with double markers in mice. Cell *121*, 479–492.
30. Hippenmeyer, S., Youn, Y.H., Moon, H.M., Miyamichi, K., Zong, H., Wynshaw-Boris, A., and Luo, L. (2010). Genetic mosaic dissection of Lis1 and Ndel1 in neuronal migration. Neuron *68*, 695–709.
31. Beattie, R., Streicher, C., Amberg, N., Cheung, G., Contreras, X., Hansen, A.H., and Hippenmeyer, S. (2020). Lineage tracing and clonal analysis in developing cerebral cortex using Mosaic Analysis with Double Markers (MADM). J. Vis. Exp. *159*, e61147.

32. Contreras, X., Amberg, N., Davaatseren, A., Hansen, A.H., Sonntag, J., Andersen, L., Bernthaler, T., Streicher, C., Heger, A., Johnson, R.L., et al. (2021). A genome-wide library of MADM mice for single-cell genetic mosaic analysis. Cell Rep. *35*, 109274.

33. Arnold, K., Sarkar, A., Yram, M.A., Polo, J.M., Bronson, R., SenGupta, S., Seandel, M., Geijsen, N., and Hochedlinger, K. (2011). Sox2(+) adult stem and progenitor cells are important for tissue regeneration and survival of mice. Cell Stem Cell *9*, 317–329.

34. Galileo, D.S., Gray, G.E., Owens, G.C., Majors, J., and Sanes, J.R. (1990). Neurons and glia arise from a common progenitor in chicken optic tectum: demonstration with two retroviruses and cell type-specific antibodies. Proc. Natl. Acad. Sci. USA *87*, 458–462.

35. Gao, P., Postiglione, M.P., Krieger, T.G., Hernandez, L., Wang, C., Han, Z., Streicher, C., Papusheva, E., Insolera, R., Chugh, K., et al. (2014). Deterministic progenitor behavior and unitary production of neurons in the neocortex. Cell *159*, 775–788.

36. Vogt, D., Cho, K.K.A., Lee, A.T., Sohal, V.S., and Rubenstein, J.L.R. (2015). The parvalbumin/somatostatin ratio is increased in Pten mutant mice and by human PTEN ASD alleles. Cell Rep. *11*, 944–956.

37. Amberg, N., and Hippenmeyer, S. (2021). Genetic mosaic dissection of candidate genes in mice using mosaic analysis with double markers. Star Protoc. *2*, 100939.

38. Groszer, M., Erickson, R., Scripture-Adams, D.D., Lesche, R., Trumpp, A., Zack, J.A., Kornblum, H.I., Liu, X., and Wu, H. (2001). Negative regulation of neural stem/progenitor cell proliferation by the Pten tumor suppressor gene in vivo. Science *294*, 2186–2189.

39. Stiles, B., Groszer, M., Wang, S., Jiao, J., and Wu, H. (2004). PTENless means more. Dev. Biol. *273*, 175–184.

40. Mize, R.R. (1992). The organization of GABAergic neurons in the mammalian superior colliculus. Prog. Brain Res. *90*, 219–248.

41. Oberst, P., Agirman, G., and Jabaudon, D. (2019). Principles of progenitor temporal patterning in the developing invertebrate and vertebrate nervous system. Curr. Opin. Neurobiol. *56*, 185–193.

42. Holguera, I., and Desplan, C. (2018). Neuronal specification in space and time. Science *362*, 176–180.

43. Greig, L.C., Woodworth, M.B., Galazo, M.J., Padmanabhan, H., and Macklis, J.D. (2013). Molecular logic of neocortical projection neuron specification, development and diversity. Nat. Rev. Neurosci. *14*, 755–769.

44. Lodato, S., and Arlotta, P. (2015). Generating neuronal diversity in the mammalian cerebral cortex. Annu. Rev. Cell Dev. Biol. *31*, 699–720.

45. Altman, J., and Bayer, S.A. (1981). Time of origin of neurons of the rat superior colliculus in relation to other components of the visual and visuomotor pathways. Exp. Brain Res. *42*, 424–434.

46. Baumann, N., Wagener, R., Javed, A., Abe, P., Lopes, A., Lavalley, A., Fuciec, D., Magrinelli, E., Fièvre, S., and Jabaudon, D. (2023). Regional differences in progenitor consumption dynamics shape brain growth during development.

47. Shen, Z., Lin, Y., Yang, J., Jörg, D.J., Peng, Y., Zhang, X., Xu, Y., Hernandez, L., Ma, J., Simons, B.D., et al. (2021). Distinct progenitor behavior underlying neocortical gliogenesis related to tumorigenesis. Cell Rep. *34*, 108853.

48. Turner, D.L., and Cepko, C.L. (1987). A common progenitor for neurons and glia persists in rat retina late in development. Nature *328*, 131–136.

49. Turner, D.L., Snyder, E.Y., and Cepko, C.L. (1990). Lineage-independent determination of cell type in the embryonic mouse retina. Neuron *4*, 833–845.

50. Gomes, F.L., Zhang, G., Carbonell, F., Correa, J.A., Harris, W.A., Simons, B.D., and Cayouette, M. (2011). Reconstruction of rat retinal progenitor cell lineages in vitro reveals a surprising degree of stochasticity in cell fate decisions. Development *138*, 227–235.

51. He, J., Zhang, G., Almeida, A.D., Cayouette, M., Simons, B.D., and Harris, W.A. (2012). How variable clones build an invariant retina. Neuron *75*, 786–798.

52. Young, R.W. (1985). Cell differentiation in the retina of the mouse. Anat. Rec. *212*, 199–205.

53. Rapaport, D.H., Rakic, P., and LaVail, M.M. (1996). Spatiotemporal gradients of cell genesis in the primate retina. Perspect. Dev. Neurobiol. *3*, 147–159.

54. Kriegstein, A., and Alvarez-Buylla, A. (2009). The glial nature of embryonic and adult neural stem cells. Annu. Rev. Neurosci. *32*, 149–184.

55. Taverna, E., Götz, M., and Huttner, W.B. (2014). The cell biology of neurogenesis: toward an understanding of the development and evolution of the neocortex. Annu. Rev. Cell Dev. Biol. *30*, 465–502.

56. Hippenmeyer, S. (2023). Principles of neural stem cell lineage progression: insights from developing cerebral cortex. Curr. Opin. Neurobiol. *79*, 102695.

57. Lim, L., Mi, D., Llorca, A., and Marín, O. (2018). Development and functional diversification of cortical interneurons. Neuron *100*, 294–313.

58. Wamsley, B., and Fishell, G. (2017). Genetic and activity-dependent mechanisms underlying interneuron diversity. Nat. Rev. Neurosci. *18*, 299–309.

59. Bandler, R.C., and Mayer, C. (2023). Deciphering inhibitory neuron development: the paths to diversity. Curr. Opin. Neurobiol. *79*, 102691.

60. Lledo, P.M., Merkle, F.T., and Alvarez-Buylla, A. (2008). Origin and function of olfactory bulb interneuron diversity. Trends Neurosci. *31*, 392–400.

61. Lim, D.A., and Alvarez-Buylla, A. (2016). The adult ventricular-subventricular zone (V-SVZ) and olfactory bulb (OB) neurogenesis. Cold Spring Harb. Perspect. Biol. *8*, a018820.

62. Achim, K., Peltopuro, P., Lahti, L., Li, J., Salminen, M., and Partanen, J. (2012). Distinct developmental origins and regulatory mechanisms for GABAergic neurons associated with dopaminergic nuclei in the ventral mesodiencephalic region. Development *139*, 2360–2370.

63. Hatten, M.E. (1999). Central nervous system neuronal migration. Annu. Rev. Neurosci. *22*, 511–539.

64. Ohtoshi, A. (2008). Hydrocephalus caused by conditional ablation of the Pten or beta-catenin gene. Cerebrospinal Fluid Res. *5*, 16.

65. Clipperton-Allen, A.E., Swick, H., Botero, V., Aceti, M., Ellegood, J., Lerch, J.P., and Page, D.T. (2022). Pten haploinsufficiency causes desynchronized growth of brain areas involved in sensory processing. iScience *25*, 103796.

66. Peng, C.Y., Yajima, H., Burns, C.E., Zon, L.I., Sisodia, S.S., Pfaff, S.L., and Sharma, K. (2007). Notch and MAML signaling drives Scl-dependent interneuron diversity in the spinal cord. Neuron *53*, 813–827.

67. Zhang, T., Liu, T., Mora, N., Guegan, J., Bertrand, M., Contreras, X., Hansen, A.H., Streicher, C., Anderle, M., Danda, N., et al. (2021). Generation of excitatory and inhibitory neurons from common progenitors via Notch signaling in the cerebellum. Cell Rep. *35*, 109208.

68. Butts, T., Green, M.J., and Wingate, R.J. (2014). Development of the cerebellum: simple steps to make a 'little brain'. Development *141*, 4031–4041.

69. Santos-França, P.L., David, L.A., Kassem, F., Meng, X.Q., and Cayouette, M. (2023). Time to see: how temporal identity factors specify the developing mammalian retina. Semin. Cell Dev. Biol. *142*, 36–42.

70. West, E.R., Lapan, S.W., Lee, C., Kajderowicz, K.M., Li, X., and Cepko, C.L. (2022). Spatiotemporal patterns of neuronal subtype genesis suggest hierarchical development of retinal diversity. Cell Rep. *38*, 110191.

71. Livesey, F.J., and Cepko, C.L. (2001). Vertebrate neural cell-fate determination: lessons from the retina. Nat. Rev. Neurosci. *2*, 109–118.

72. Sanes, J.R., and Zipursky, S.L. (2010). Design principles of insect and vertebrate visual systems. Neuron *66*, 15–36.

73. Rompani, S.B., and Cepko, C.L. (2008). Retinal progenitor cells can produce restricted subsets of horizontal cells. Proc. Natl. Acad. Sci. USA *105*, 192–197.

74. Hafler, B.P., Surzenko, N., Beier, K.T., Punzo, C., Trimarchi, J.M., Kong, J.H., and Cepko, C.L. (2012). Transcription factor Olig2 defines subpopulations of retinal progenitor cells biased toward specific cell fates. Proc. Natl. Acad. Sci. USA *109*, 7882–7887.

75. Wang, S., Sengel, C., Emerson, M.M., and Cepko, C.L. (2014). A gene regulatory network controls the binary fate decision of rod and bipolar cells in the vertebrate retina. Dev. Cell *30*, 513–527.

76. Petersen, P.H., Zou, K., Hwang, J.K., Jan, Y.N., and Zhong, W. (2002). Progenitor cell maintenance requires numb and numblike during mouse neurogenesis. Nature *419*, 929–934.

77. Hippenmeyer, S., Vrieseling, E., Sigrist, M., Portmann, T., Laengle, C., Ladle, D.R., and Arber, S. (2005). A developmental switch in the response of DRG neurons to ETS transcription factor signaling. PLOS Biol. *3*, e159.

78. Schindelin, J., Arganda-Carreras, I., Frise, E., Kaynig, V., Longair, M., Pietzsch, T., Preibisch, S., Rueden, C., Saalfeld, S., Schmid, B., et al. (2012). Fiji: an open-source platform for biological-image analysis. Nat. Methods *9*, 676–682.

79. Hao, Y., Hao, S., Andersen-Nissen, E., Mauck, W.M., 3rd, Zheng, S., Butler, A., Lee, M.J., Wilk, A.J., Darby, C., Zager, M., et al. (2021). Integrated analysis of multimodal single-cell data. Cell *184*, 3573–3587.e29.

80. Cao, J., Spielmann, M., Qiu, X., Huang, X., Ibrahim, D.M., Hill, A.J., Zhang, F., Mundlos, S., Christiansen, L., Steemers, F.J., et al. (2019). The single-cell transcriptional landscape of mammalian organogenesis. Nature *566*, 496–502.

81. McCarthy, D.J., Campbell, K.R., Lun, A.T., and Wills, Q.F. (2017). Scater: pre-processing, quality control, normalization and visualization of single-cell RNA-seq data in R. Bioinformatics *33*, 1179–1186.

82. Haghverdi, L., Lun, A.T.L., Morgan, M.D., and Marioni, J.C. (2018). Batch effects in single-cell RNA-sequencing data are corrected by matching mutual nearest neighbors. Nat. Biotechnol. *36*, 421–427.

83. La Manno, G., Soldatov, R., Zeisel, A., Braun, E., Hochgerner, H., Petukhov, V., Lidschreiber, K., Kastriti, M.E., Lönnerberg, P., Furlan, A., et al. (2018). RNA velocity of single cells. Nature *560*, 494–498.

84. Bergen, V., Soldatov, R.A., Kharchenko, P.V., and Theis, F.J. (2021). RNA velocity-current challenges and future perspectives. Mol. Syst. Biol. *17*, e10282.

85. Dobin, A., Davis, C.A., Schlesinger, F., Drenkow, J., Zaleski, C., Jha, S., Batut, P., Chaisson, M., and Gingeras, T.R. (2013). STAR: ultrafast universal RNA-seq aligner. Bioinformatics *29*, 15–21.

86. Gu, X., He, D., Li, Y., Hu, C., Wei, Y.S., Liu, G., Liu, D., Pleasure, S.J., Xie, W., and Zhao, C. (2008). Generation of Frizzled10-Cre transgenic mouse line: a useful tool for the study of dorsal telencephalic development. Genesis *46*, 523–529.

87. Nunnally, A.P., and Parr, B.A. (2004). Analysis of Fz10 expression in mouse embryos. Dev. Genes Evol. *214*, 144–148.

88. Summerhurst, K., Stark, M., Sharpe, J., Davidson, D., and Murphy, P. (2008). 3D representation of Wnt and Frizzled gene expression patterns in the mouse embryo at embryonic day 11.5 (Ts19). Gene Expr. Patterns *8*, 331–348.

89. Feil, R., Wagner, J., Metzger, D., and Chambon, P. (1997). Regulation of Cre recombinase activity by mutated estrogen receptor ligand-binding domains. Biochem. Biophys. Res. Commun. *237*, 752–757.

90. Arber, S., Han, B., Mendelsohn, M., Smith, M., Jessell, T.M., and Sockanathan, S. (1999). Requirement for the homeobox gene Hb9 in the consolidation of motor neuron identity. Neuron *23*, 659–674.

91. Laukoter, S., Amberg, N., Pauler, F.M., and Hippenmeyer, S. (2020). Generation and isolation of single cells from mouse brain with mosaic analysis with double markers-induced uniparental chromosome disomy. Star Protoc. *1*, 100215.

92. Cadwell, C.R., Scala, F., Li, S., Livrizzi, G., Shen, S., Sandberg, R., Jiang, X., and Tolias, A.S. (2017). Multimodal profiling of single-cell morphology, electrophysiology, and gene expression using Patch-seq. Nat. Protoc. *12*, 2531–2553.

93. Cadwell, C.R., Scala, F., Fahey, P.G., Kobak, D., Mulherkar, S., Sinz, F.H., Papadopoulos, S., Tan, Z.H., Johnsson, P., Hartmanis, L., et al. (2020). Cell type composition and circuit organization of clonally related excitatory neurons in the juvenile mouse neocortex. eLife *9*.

94. Picelli, S., Faridani, O.R., Björklund, A.K., Winberg, G., Sagasser, S., and Sandberg, R. (2014). Full-length RNA-seq from single cells using Smart-seq2. Nat. Protoc. *9*, 171–181.

95. Hippenmeyer, S. (2013). Dissection of gene function at clonal level using mosaic analysis with double markers. Front. Biol. *8*, 557–568.

96. Beattie, R., Postiglione, M.P., Burnett, L.E., Laukoter, S., Streicher, C., Pauler, F.M., Xiao, G., Klezovitch, O., Vasioukhin, V., Ghashghaei, T.H., et al. (2017). Mosaic analysis with double markers reveals distinct sequential functions of Lgl1 in neural stem cells. Neuron *94*, 517–533.e3.

97. Lee, B.R., Budzillo, A., Hadley, K., Miller, J.A., Jarsky, T., Baker, K., Hill, D., Kim, L., Mann, R., Ng, L., et al. (2021). Scaled, high fidelity electrophysiological, morphological, and transcriptomic cell characterization. eLife *10*.

98. Berg, J., Sorensen, S.A., Ting, J.T., Miller, J.A., Chartrand, T., Buchin, A., Bakken, T.E., Budzillo, A., Dee, N., Ding, S.L., et al. (2021). Human neocortical expansion involves glutamatergic neuron diversification. Nature *598*, 151–158.

99. Suzuki, R., and Shimodaira, H. (2006). Pvclust: an R package for assessing the uncertainty in hierarchical clustering. Bioinformatics *22*, 1540–1542.

STAR★METHODS

KEY RESOURCES TABLE

REAGENT or RESOURCE	SOURCE	IDENTIFIER
Antibodies		
GFP–Chicken	Aves Labs Inc.	Cat#GFP-1020; RRID:AB_10000240
RFP–Rabbit	MBL	Cat#PM005; RRID:AB_591279
tdTomato–Goat	Sicgen Antibodies	Cat#AB8181-200; RRID:AB_2722750
β-galactosidase–Chicken	Abcam	Cat#ab9361; RRID:AB_307210
Ki67–Rabbit	Abcam	Cat#ab15580; RRID:AB_443209
DCX–Rabbit	Abcam	Cat#ab18723; RRID:AB_732011
Olig2–Rabbit	Millipore	Cat#AB9610; RRID:AB_570666
NeuN-Mouse	Millipore	Cat#MAB377; RRID:AB_229872
Sox9-Rabbit	Cell Signaling	Cat#Ab#82630; RRID:AB_2665492
Anti-chicken-Alexa 488	Jackson ImmunoResearch Labs	Cat#703-545-155; RRID:AB_2340375
Anti-rabbit-Alexa568	Thermo Fisher Scientific	Cat#A10042; RRID:AB_2534017
Anti-rabbit-Alexa647	Thermo Fisher Scientific	Cat#A31573; RRID:AB_2536183
Anti-goat-Alexa568	Thermo Fisher Scientific	Cat#A11057; RRID:AB_2534104
Anti-goat-Alexa647	Thermo Fisher Scientific	Cat#A21447; RRID:AB_2535864
Anti-mouse-Alexa647	Thermo Fisher Scientific	Cat#A31571; RRID:AB_162542
DAPI	Thermo Fisher Scientific	Cat#D1306; RRID:AB_2629482
Chemicals, peptides, and recombinant proteins		
Papain Vial	Worthington	Cat#LK003178
DNase Vial	Worthington	Cat#LK003172
Ovomucoid Inhibitor Vial	Worthington	Cat#LK003182
EBSS (Earle's Balanced Salt Solution)	Thermo Fisher Scientific	Cat#24010043
DMEM/F12	Thermo Fisher Scientific	Cat#21041025
HBSS (Hanks' Balanced Salt Solution)	Thermo Fisher Scientific	Cat#14175095
DPBS (Dulbecco's Phosphate Buffered Saline)	Thermo Fisher Scientific	Cat#14190094
RNase free water	Thermo Fisher Scientific	Cat#10977035
RNase Away	Thermo Fisher Scientific	Cat#10328011
RNase Inhibitor	Takara Bio	Cat#2313A
Debris Removal Solution	Miltenyi Biotec	Cat#130-109-398
DEPC (diethyl pyrocarbonate)	Sigma-Aldrich	Cat#D5758
Zombie NIR fixable viability dye	Biolegend	Cat#423105
Mowiol 4-88	Carl Roth	Cat#0713.2
DABCO (1,4-diazabicyclooctane)	Carl Roth	Cat#0718.2
Critical commercial assays		
SMART-Seq Single Cell PLUS Kit, 48 rxns	Takara Bio	Cat#R400750
Next GEM Single Cell 3' Reagent Kit v.3.1, 16 rxns	10X Genomics	Cat#PN1000121
Deposited data		
Pten$^{+/+}$ and *Pten*$^{-/-}$ scRNA-Seq	This study	GEO: GSE245104
Fzd10 embryo pool scRNA-Seq	This study	GEO: GSE245105
E10 MADM-CloneSeq	This study	GEO: GSE245102
E12 MADM-CloneSeq	This study	GEO: GSE245103
Experimental models: Organisms/strains		
Mouse: *MADM-11-GT*	The Jackson Laboratory Hippenmeyer et al.[30]	RRID:IMSR_JAX:013749

(*Continued on next page*)

Continued

REAGENT or RESOURCE	SOURCE	IDENTIFIER
Mouse: *MADM-11-TG*	The Jackson Laboratory Hippenmeyer et al.[30]	RRID:IMSR_JAX:013751
Mouse: *MADM-19-GT*	European Mouse Mutant Archive (EMMA) Contreras et al.[32]	RRID:IMSR_EM:14720
Mouse: *MADM-19-TG*	European Mouse Mutant Archive (EMMA) Contreras et al.[32]	RRID:IMSR_EM:14721
Mouse: mTmG	The Jackson Laboratory Muzumdar et al.[28]	RRID:IMSR_JAX:007676
Mouse: *Pten^{flox}*	The Jackson Laboratory Groszer et al.[38]	RRID:IMSR_JAX:004597
Mouse: *Nestin-Cre*	Petersen et al.[76]	N/A
Mouse: *Sox2^{CreER}*	The Jackson Laboratory Arnold et al.[33]	RRID:IMSR_JAX:017593
Mouse: *Tau^{mGFP}*	The Jackson Laboratory Hippenmeyer et al.[77]	RRID:IMSR_JAX:021162
Mouse: *Fzd10-CreER*	This study	N/A
Software and algorithms		
ZEN Digital Imaging for Light Microscopy – Blue 2.3 and 2.6	Zeiss	https://www.zeiss.com/microscopy/en/products/software/zeiss-zen.html RRID:SCR_013672
Graphpad Prism 8.0	GraphPad	https://www.graphpad.com/scientific-software/prism/ RRID:SCR_002798
Fiji (v1.53)	Schindelin et al.[78]	https://fiji.sc/ RRID:SCR_002285
Cellranger (v7.0.0)	10X Genomics	https://www.10xgenomics.com/ RRID:SCR_017344
R (v4.0.3/4.1.2/4.2.1)	R Project for Statistical Computing	https://www.r-project.org/ RRID:SCR_001905
loomR (v0.2.1)	N/A	https://github.com/mojaveazure/loomR
Seurat (v4.0.4/4.1.0/4.2.0)	Hao et al.[79]	https://github.com/satijalab/seurat RRID:SCR_016341
GenBinomApps v1.1/1.2	N/A	https://cran.r-project.org/package=GenBinomApps
monocle3 (v1.2.9)	Cao et al.[80]	https://cole-trapnell-lab.github.io/monocle3/ RRID:SCR_018685
SeuratWrappers (v0.3.1)	N/A	https://github.com/satijalab/seurat-wrappers RRID:SCR_022555
scater (v1.18.6)	McCarthy et al.[81]	https://bioconductor.org/ RRID:SCR_015954
batchelor (v1.6.3)	Haghverdi et al.[82]	https://bioconductor.org/
pheatmap (v1.0.12)	N/A	https://cran.r-project.org/package=pheatmap
pvclust package (v2.2.0)	N/A	https://cran.r-project.org/package=pvclust
velocyto (v0.17.17)	La Manno et al.[83]	https://velocyto.org RRID:SCR_018167
scvelo (v0.2.4)	Bergen et al.[84]	https://github.com/theislab/scvelo RRID:SCR_018168
STAR (v.2.7.9a)	Dobin et al.[85]	https://github.com/alexdobin/STAR RRID:SCR_004463
BZ-II Viewer software	Keyence	N/A

(*Continued on next page*)

Continued

REAGENT or RESOURCE	SOURCE	IDENTIFIER
CellSens software	Olympus	https://www.olympus-lifescience.com/en/software/cellsens/ RRID:SCR_014551
SH800 Cell Sorter software	SONY	https://www.sonybiotechnology.com/us/instruments/sh800s-cell-sorter/software/
Scripts generated in this study	This study	https://github.com/fpauler/Multipotent-Progenitors-Instruct-Ontogeny-of-the-Superior-Colliculus https://doi.org/10.5281/zenodo.10089056 (https://zenodo.org/records/10089056)
Other		
Cryostat Cryostar NX70	Thermo Fisher Scientific	https://www.thermofisher.com
Zeiss Axio Imager 2 Microscope	Zeiss	https://www.zeiss.com/microscopy/en/products/light-microscopes.html RRID:SCR_018876
Zeiss LSM 800 Confocal Microscope	Zeiss	https://www.zeiss.com/microscopy/en/products/light-microscopes/confocal-microscopes.html
Sony SH800 Cell Sorter	Sony	https://www.sonybiotechnology.com/us/instruments/sh800s-cell-sorter/ RRID:SCR_018066
Dosaka Linear-Pro7 vibratome	Dosaka	https://www.dosaka-em.jp/haiban/495/
Keyence BZ-9000E inverted fluorescence microscope	Keyence	https://www.keyence.de/products/microscope/fluorescence-microscope/bz-9000/models/bz-9000e/
Olympus BX51WI microscope	Olympus	https://www.olympus-lifescience.com/en/microscopes/upright/bxwi/ RRID:SCR_023069
Olympus XM10 Camera	Olympus	https://www.olympus-ims.com/en/microscope/xm10/
Sutter P-1000 Micropipette Puller	Sutter Instrument	https://www.sutter.com/MICROPIPETTE/p-1000.html RRID:SCR_021042
NovaSeq 6000	Illumina	https://www.illumina.com/systems/sequencing-platforms/novaseq.html RRID:SCR_016387

RESOURCE AVAILABILITY

Lead contact

Any additional information required to reanalyze the data reported in this paper is available from the lead contact upon request.

Materials availability

All reagents and mouse lines generated in this study will be shared upon request within the limits of the respective material transfer agreements. All MADM lines used in this study are publicly available through The Jackson Laboratory, The European Mouse Mutant Archive (EMMA) and distributed from the University of Veterinary Medicine in Vienna or the Institute of Science and Technology Austria in Klosterneuburg in Austria.

Data and code availability

All data generated and analyzed in this study are included in the paper and/or supplementary materials. Raw sequencing data has been deposited at Gene Expression Omnibus (GEO). All scripts that were used to prepare data and figures for this manuscript are available via GitHub at https://github.com/fpauler. Accession numbers and github DOI are listed in the key resources table. Files for 3D printing of acute slice recovery chamber (3D model 361319) are deposited to https://www.printables.com.

EXPERIMENTAL MODEL AND SUBJECT DETAILS

Mice

All animal procedures were approved by the Austrian Federal Ministry of Science and Research in accordance with the Austrian and European Union animal law (license number: BMWF-66.018/0007-II/3b/2012 and BMWFW-66.018/0006-WF/V/3b/2017). Experimental mice were bred and maintained according to regulations approved by institutional animal care and use committee, institutional ethics committee and the guidelines of the preclinical facility (PCF) at IST Austria. Mice were housed at 21±1°C ambient temperature and 40-55% humidity in 12 hrs dark/light cycles. Transgenic mouse lines with MADM cassettes inserted in Chr.11[30] and Chr.19,[32] *Sox2*^{CreER},[33] *Nestin-Cre*,[76] *mTmG* reporter,[28] *Pten*-flox[38] have been previously described. All mouse lines were kept in mixed C57/Bl6, FVB and CD1 genetic background. In some experiments, wild-type CD1 mice were also used. Both male and female littermates of the desired genotypes were used randomly. Mice were used at an age range from 2-8 months for breeding and from E9.5 to P30 for experiments. All efforts were made to minimize the number of animals used following the 3R principles.

METHOD DETAILS

Generation of Experimental Mice

Fzd10-CreER$^{+/-}$ *transgenic mice*

While in search for a promoter that drives midbrain-specific expression in mouse embryos, we were inspired by previous work using the promoter of *Fzd10*, a Wnt receptor, to drive expression in several posterior brain regions including the dorsal part of the midbrain and thalamus.[86] *Fzd10* is highly expressed endogenously in the developing midbrain from as early as E9.5.[87] Interestingly, *Fzd10* is also the only *Fzd* isoform expressed in the midbrain that is not also expressed in the cortex.[88] In an effort to more faithfully/cleanly recapitulate endogenous expression pattern in this study, we generated a *Fzd10-CreER* transgene using a slightly larger promoter fragment than previously used.[86] *Fzd10-CreER*$^{+/-}$ transgenic mice were generated as follows. A 9.5 kb fragment containing upstream promoter region of mouse *Frizzled10* (*Fzd10*) gene was subcloned into pGEM vector (Promega). *CreER*^{T2} gene,[89] a gift from K. Miyamichi, was inserted in frame with the endogenous start ATG of *Fzd10*. Immediately downstream of *CreER*^{T2}, a cassette comprised of an *IRES-taulacZ* followed by SV40 polyadenylation signal,[90] gift from S. Arber, was inserted. The final *Fzd10-CreERT2-IRES-TLZ* transgene fragment was excised from the modified vector with *PmeI* and *AscI*, purified by agarose gel electrophoresis followed by QIAEX II (Qiagen), and injected into pronuclei of fertilized one-cell eggs from FVB at the Stanford Transgenic Facility. In total, seven *Fzd10-CreER*$^{+/-}$ transgenic founders were identified by PCR genotyping using *Cre*-specific primers. Upon assessment of TM (Sigma-Aldrich)-induced recombination in *Tau::mGFP* reporter,[77] one line (2#5) was maintained for all further investigation in this study.

mTmG;Fzd10-CreER$^{+/-}$ *mice for scRNA-seq experiments*

To selectively label and isolate cells of the *Fzd10*-lineage in the embryonic dorsal midbrain, *Fzd10-CreER*$^{+/-}$ mice were crossed with *mTmG* reporter line to generate *mTmG;Fzd10-CreER*$^{+/-}$ embryos. Timed pregnant females received intraperitoneal (IP) injections of TM (1 mg/mouse dissolved in corn oil) at E10.5. Upon *Cre* activation, a switch of fluorescent color from red (tdT) to green (GFP), according to the *mTmG* principle[28] was observed in the embryonic midbrain cells (Figures S2I–S2K). Dorsal midbrain from these *mTmG;Fzd10-CreER*$^{+/-}$ embryos were isolated at E12.5, E14.5 and E16.5 for scRNA-seq experiments.

Mice containing SC MADM clones

MADM clone induction in SC was adapted from previously described protocols.[30,31] In brief, *MADM-11*$^{GT/TG}$*;CreER* mice were generated by crossing *MADM-11*$^{GT/GT}$*;CreER* with *MADM-11*$^{TG/TG}$ mice (Figure S3A). Two inducible *Cre* drivers (*Sox2*-CreER and *Fzd10*-CreER) were used independently to generate SC MADM clones. To induce MADM clones, timed pregnant females were IP injected with TM (1-2 mg/mouse dissolved in corn oil) at E9.5, 10.5, 11.5, or 12.5, respectively. At E19.5, litters were delivered by caesarean section and raised with foster females. Experimental mice were collected for analysis between P28-P30 (Figure S3B). In total, we obtained 268 clones from 273 brains which equals to an overall average of 0.982 clone/brain (126 clones/131 *Fzd10-CreER*$^{+/-}$ brains and 142 clones/142 *Sox2*$^{CreER/+}$ brains).

Control-MADM and Pten*-MADM mice*

To generate MADM genetic mosaic mice for *Pten* gene, we followed previously established protocols.[32,37] In brief, the *Pten*-flox allele was recombined onto Chr.19 containing the MADM-TG cassette to generate *MADM-19*$^{TG/TG,Pten\text{-}flox}$ stocks. Next, *MADM-19*$^{TG/TG,Pten\text{-}flox}$ were crossed with *MADM-19*$^{GT/GT}$*;Nestin-Cre*$^{+/-}$ to generate Control-MADM (*MADM-19*$^{GT/TG}$*;Nestin-Cre*$^{+/-}$) and *Pten*-MADM (*MADM-19*$^{GT/TG,Pten\text{-}flox}$*;Nestin-Cre*$^{+/-}$) mice (Figure S8B). Upon *Cre* recombinase-mediated interchromosomal recombination for reconstitution of fluorescent MADM markers, all (red tdT^{+}, green GFP^{+} and yellow tdT^{+}/GFP^{+}) cells in Control-MADM were wild-type (*Pten*$^{+/+}$) whereas in *Pten*-MADM red tdT^{+} cells were wild-type (*Pten*$^{+/+}$), green GFP^{+} cells homozygous mutant (*Pten*$^{-/-}$) and yellow tdT^{+}/GFP^{+} cells heterozygous (*Pten*$^{+/-}$) in an otherwise unlabeled *Pten*$^{+/-}$ environment (Figures 6A–6C and S8C). Control-MADM and *Pten*-MADM brain samples were collected at P0 and P28 for histological studies; and at P0 for scRNA-seq experiments. For scRNA-seq experiments, only green *Pten*$^{+/+}$ and green *Pten*$^{-/-}$ cells were collected from Control-MADM and *Pten*-MADM, respectively.

Single-cell RNA Sequencing

Preparation of single-cell suspension

Embryonic dorsal midbrains were dissected at E12.5, E14.5 and E16.5 by first cutting the skin and skull to expose the dorsal part of the brain. An incision was made between the forebrain-midbrain boundary and another one between the midbrain-hindbrain boundary with fine surgical scissors. Two horizontal cuts were then made through the aqueduct to free the dorsal midbrains. In total, 9, 8, and 3 dorsal midbrains were pooled for each of E12.5, E14.5 and E16.5 time points, respectively. To isolate P0 dorsal midbrains, mice were first decapitated and the brains dissected from the skull. After removing the cortices to expose the midbrain, two cuts were made with sharp razor blades: one between the forebrain-SC boundary and another between the SC-inferior colliculus boundary. Both cuts were angled to meet at the aqueduct thus avoiding contamination from ventral midbrain regions. In total, 26 Control-MADM and 24 *Pten*-MADM dorsal midbrains were separately pooled. The subsequent preparation procedures of single-cell suspension from these tissues were adapted and modified from previous protocols.[91] Dissected tissues were first incubated in Earle's Balanced Salt Solution (EBSS, Thermo Fischer Scientific) containing Papain (Worthington) and DNaseI (Worthington) for 30 mins at 37°C with gentle shaking at 150rpm. After adding Ovomucoid I-Albumin (Worthington), tissue suspension was briefly dissociated mechanically with a pipette. After centrifugation at 1000rpm for 10 mins at room temperature, cell pellet was re-suspended and further mechanically dissociated until a homogeneous cell suspension was obtained. A second centrifugation at 1500rpm for 10 mins at room temperature produced the final pellet for fluorescence-activated cell sorting (FACS) for embryonic samples. P0 samples were processed further to remove debris due to an increased amount of myelination in the midbrain at this time point. Cell pellets were re-suspended and mixed with cold Debris Removal Solution (Miltenyi Biotec). The mixture was carefully overlaid with cold PBS before centrifugation at 3000 x g for 10 mins at 4°C. The top two layers containing PBS and debris were then aspirated and removed. The remaining cleaned cell suspension was then collected by a last centrifugation at 1000 x g for 10 mins at 4°C for FACS. Single-cell suspensions were incubated with Zombie NIR fixable viability dye (Biolegend) and viable GFP^+ cells were sort-purified immediately using a SH800 Cell Sorter (Sony). In total, 33,000 labeled cells were collected from each embryonic time point while 14,000 and 12,000 labeled cells were sorted from P0 time point of Control-MADM and *Pten*-MADM, respectively. All cells were sorted in freshly prepared cold DMEM (Thermo Fisher Scientific) supplemented with fetal bovine and horse serum (Thermo Fisher Scientific) and processed immediately.

Preparation of cDNA libraries and scRNA-seq

cDNA libraries were generated from Control-MADM, *Pten*-MADM, and pooled embryonic dorsal midbrain samples containing *Fzd10*-lineage cells using the Chromium Controller and the Next GEM Single Cell 3' Reagent Kit (v3.1, 10x Genomics) according to the manufacturer's instructions. Libraries were sequenced by the Biomedical Sequencing Facility at the CeMM Research Center for Molecular Medicine of the Austrian Academy of Sciences, using the Illumina NovaSeq 6000 platform. Raw sequencing data was pre-processed and demultiplexed using bcl2fastq (v 2.20.0.422).

Collection of MADM-labeled Tissue for Histological Studies

Tissue collection and cryosectioning

Tissue collection for histological studies was performed according to previously described protocols.[31] For the collection of embryonic tissues, the embryos were dissected at specific developmental time points. P0 mice were collected on the day of natural birth. Brains were dissected after decapitation of mice and fixed in 4% PFA (paraformaldehyde; Sigma-Aldrich) overnight at 4°C. For the collection of postnatal tissues, mice at P28-P30 were first anesthetized by a mixture of ketamine (65mg/kg), xylazine (13mg/kg) and acepromazine (2mg/kg) by IP injection. Transcardial perfusion of mice was performed with ice-cold PBS (phosphate-buffered saline) followed by ice-cold 4% PFA using a peristatic pump (Carl Roth, 4-6ml/min). Perfused brains were removed from the skull and post-fixed in 4% PFA overnight at 4°C. Upon complete fixation, both embryonic and postnatal brains were transferred to 30% sucrose solution (Sigma-Aldrich, dissolved in PBS) for 48-72 hrs. Tissues were embedded in Tissue-Tek O.C.T. (Sakura) and stored at -20°C or -80°C until further use. For histological analysis, both embryonic and postnatal embedded tissues were cryosectioned using CryoStar NX70 cryostat (Thermo Fisher Scientific). Embryonic tissues were sectioned in either coronal or sagittal orientation at 20-30μm thickness and directly mounted onto superfrost glass slides (Thermo Fisher Scientific). Postnatal tissues were cryosectioned in coronal orientation at 30-45μm thickness and first collected in PBS and then mounted onto glass slides. For brains containing MADM clones in SC sections were collected, and kept in the same left-right orientation and in serial order, in multiple 24-well plates containing PBS. Mounted sections were air dried while protected from light and processed immediately for analysis.

Immunostaining

For immunostaining procedures, cryosections mounted on glass slides were first rehydrated with PBS at room temperature for 15 mins whereas acute brain slices (see below) were kept floating in PBS in multi-well plates to optimize permeability. Tissues were blocked for 2 hrs at room temperature in blocking solution. For cryosections we used 0.5% Triton X-100 with 5% Donkey Serum (Thermo Fisher Scientific) in PBS. For acute brain slices 1.2% Triton X-100 with 5% Donkey Serum in PBS was used. For some antibodies, an additional antigen retrieval incubation (Citrate Buffer; 192M citric acid + 0.05% Tween20; pH 6.0; at 85°C for 25 mins) was performed prior to adding blocking solution. After blocking, tissues were incubated for 16-48 hrs at 4°C with primary antibodies diluted in blocking solution. After washing with PBS with Triton X-100 (PBT), tissues were treated for 2 hrs at room temperature with secondary antibodies diluted in PBT. Finally, cell nuclei were stained with DAPI (4',6-diamidino-2-phenylindole, Thermo Fisher

Scientific, 1:5000 dilution) for 15 mins. Acute slices were mounted on glass slides and allowed to dry. All sections were mounted using Mowiol 4-88 (Carl Roth) and 1,4-diazabicyclooctane (DABCO; Carl Roth) and stored at 4°C until image acquisition.

Antibodies

The following primary antibodies were used: chicken anti-GFP (Aves, GFP1020, 1:500), rabbit anti-RFP (MBL, PM005, 1:500), goat anti-tdTomato (SICgen, ab8181-200, 1:500), chicken anti-beta galactosidase (Abcam, ab9361, 1:1000), rabbit anti-Ki67 (Abcam, ab15580, 1:500), rabbit anti-DCX (Abcam, ab18723, 1:200), mouse anti-NeuN (Millipore, MAB377, 1:100), rabbit anti-Sox9 (Cell Signaling, 82630, 1:100), and rabbit anti-olig2 (Millipore, AB9610, 1:200). The following secondary antibodies were used: donkey anti-chicken-Alexa488 (Jackson Immuno, 703-545-155, 1:1000), donkey anti-rabbit-Alexa568 (Life Technologies, A10042, 1:1000), donkey anti-goat-Alexa568 (Invitrogen, A11057, 1:1000), donkey anti-rabbit-Alexa647 (Life Technologies, A31573, 1:1000), donkey anti-goat-Alexa647 (Life Technologies, A21447, 1:1000), and donkey anti-mouse-Alexa647 (Life Technologies, A31571, 1:1000).

Image acquisition and processing

Before image acquisition of sparsely-labeled MADM clones in SC, mounted serial sections were first screened for clones using an axioscope (Zeiss Axio Imager, Zeiss) coupled to a CoolLED p300 SB light source (CoolLED) and equipped with Plan-Apochromat 10x/0.45 and 20x/0.8 objectives (Zeiss). Green and red fluorescence were observed using an HC-dualband GFP/DsRed filter (F56-420, AHF). The presence of MADM-labeled cells in SC was documented for subsequent confocal image acquisition. Confocal image acquisition was performed using LSM 800 series inverted confocal microscopes (Zeiss) and analyzed using ZEN Blue 2.3 and 2.6 software (Zeiss). Confocal images were acquired in z-stacks and tiles with excitation lasers 405, 488, 561, and 640nm. Plan-Apochromat 10x/0.45 and 20x/0.8 objectives were used. In order to allow accurate post-acquisition image alignment of clones spanning across multiple serial sections, the entire dorsal midbrain hemisphere consisting of SC, PAG, midline and aqueduct were included in the image. Tiled images were subsequently stitched and exported in .tif format as either z-stacks or orthogonal projections using ZEN Blue built-in processing functions.

MADM-CloneSeq

Acute brain slice preparation and screening for MADM clones

MADM-11$^{GT/TG}$;CreER experimental mice containing MADM clones in SC at P28-P30 were first deeply anesthetized via IP injection of a mixture of ketamine (90mg/kg) and xylazine (4.5mg/kg), followed by transcardial perfusion with ice-cold, oxygenated (95% O_2, 5% CO_2) artificial cerebrospinal fluid (ACSF) containing (in mM): 118 NaCl, 2.5 KCl, 1.25 NaH_2PO_4, 1.5 $MgSO_4$, 1 $CaCl_2$, 10 Glucose, 3 Myo-inositol, 30 Sucrose, 30 $NaHCO_3$ prepared in diethyl pyrocarbonate (DEPC; Sigma-Aldrich)-treated water; pH=7.4. The brain was rapidly dissected and coronal slices of 200 μm thickness including SC were cut using a Linear-Pro7 vibratome (Dosaka, Japan). To preserve left-right orientation, each brain was marked on the ventral part of one hemisphere with a clean razorblade. Individual slices containing SC were first screened on both sides for the presence of MADM-labeled cells using an inverted fluorescence phase-contrast microscope (BZ-9000E; Keyence, Japan). Images were captured and processed using BZ-II Viewer (Keyence, Japan) for documentation and also used post-hoc to locate cells for collection. Screened slices containing SC MADM clones were returned to a custom-made multi-well recovery chamber (designed and 3D-printed by Robert Beattie, https://www.printables.com, 3D model 361319) and left to recover for 20 mins at 35°C, followed by a slow cool down to room temperature over 40-60 mins.

MADM-CloneSeq sample collection

The sample collection steps for MADM-CloneSeq were adapted from previously published protocols[92,93] and optimized for speed and coverage of sparsely-labeled cells of MADM clones. To prevent RNA degradation, all solutions were prepared using water pre-treated with DEPC. All work surface and equipment were cleaned using RNase away solution (Thermo Fisher Scientific) prior to experiments. Single acute slice containing MADM clones was first transferred to a BX51WI microscope (Olympus, Tokyo, Japan) and superfused with ACSF at a rate of 1-2 ml/min at room temperature. Individual neurons were visualized under a 60x objective via infrared / differential interference contrast (IR/DIC) video system using an XM10 camera (Olympus) and cellSens software (Olympus). To observe red or green fluorescence, light was emitted from a pE-300 LED light source (CoolLED, Andover, UK). Glass pipettes (B150-86-10, Sutter Instrument, Novato, CA) previously treated with DEPC and dried at 80°C were pulled using a P-1000 pipette puller (Sutter Instrument) to generate pipettes with opening of around 3-5μm or 1-3MΩ. Immediately before use, each pipette was filled with 3μl of pipette solution which consisted of RNase inhibitor (Takara, 5% for collection from E10 clones and 0.4% for collection from E12 clones) in RNase-free PBS (Invitrogen) filtered through a 0.22μm filter. Red or green fluorescent neurons were approached with the pipette under positive pressure to avoid tissue contamination of the pipette tip. Each cell was approached from around 45° angle above the surface. When contact with cell membrane was made, tight seal formation was achieved under IR/DIC visualization. The complete aspiration of the cell body was immediately performed by applying a gentle and steady suction while monitoring under fluorescence and typically takes 5-10 s. The negative pressure was removed immediately once the target cell was collected and the pipette was carefully withdrawn from the acute slice to avoid contamination. For the collection from E10 clones, the content of each pipette was mixed with 1μl of 0.8% Triton-X (final concentration of 0.2% Triton-X, Sigma-Aldrich) and then stored in individual wells of 96-well plates. For the collection from E12 clones, the content of each pipette was directly transferred into individual PCR tubes. In both cases, samples were kept at -80°C until cDNA library preparation. At the end of sample collection, all acute slices which

contained the whole or part of a clone were fixed in 4% PFA at 4°C overnight. Fixed acute slices were then washed in and transferred to PBS and stored at 4°C until batch immunostaining procedures to reconstruct clones. See section on Immunostaining.

Preparation of cDNA libraries and RNA-seq

Individual MADM-CloneSeq cells were subsequently processed for RNA-seq. cDNA libraries from E10 clones were prepared followed by Smart-seq2 protocol[94] using custom reagents (VBCF GmbH). cDNA libraries from E12 clones were prepared using SMART-Seq Single Cell PLUS Kit (Takara). Pools of libraries were sequenced on Illumina platforms at the VBCF NGS Unit (https://www.viennabiocenter.org/facilities/).

QUANTIFICATION AND STATISTICAL ANALYSIS

MADM Clonal Analysis and 3D Reconstruction of Clones

MADM-clonal analysis using *MADM-11* transgenic lines has been previously validated to sparsely target single dividing progenitors giving rise to distinct clusters of cells each representing individual clonal units.[31,35,95,96] In particular, nearest-neighbor distance analysis was used to confirm clonality in sparse induction paradigm.[35] In the present study, an average nearest distance between two clonally-related cells of 158±6μmm (n=160 clones) was within the reported range.[35] Furthermore, high confidence of sparseness in labeling is attributed to the rare occurrence of MADM events in combination with a very low level of *CreER* activity. Here, we have titrated the dose of TM to1-2mg per mouse to obtain an average of less than one (0.982) cluster of MADM-labeled cells per brain. In the case when more than one cell clusters were found in the same brain, a 300μm minimum distance of separation was used as criteria to spatially distinguish separate clones. Taken together, the above validations support the notion of very low probability of simultaneously targeting multiple RGPs in close proximity.

Serial confocal z-stacks of each MADM clone in SC were first aligned in Fiji software v1.53[78] using custom-generated macro. The macro relied on user input to define a line ROI in the middle of each stack to be aligned against the previous stack. User input included the manual drawing of a straight line from the dorsal most border of the aqueduct along the midline using the *Straight line tool*. Upon execution of the macro, the first stack would be rotated such that the midline was exactly vertical. Subsequent stacks were rotated in the same manner and then shifted in the x- and y- dimension such that the aqueduct aligned with the previous stack. The macro automatically saved individual aligned stacks, an aligned stack of the complete clone and its maximum z-projection. After image alignment, initial data analysis involved counting of the number of red and green cells per clone. Next, the 3D coordinates of each cell were marked using Fiji *Point tool* and saved in *ROI manager*. For each clone, a reference point (x=0, y=0, z=0) was always set to the dorsal most point of the aqueduct in the middle z-plane of the clone. Apart from the 3D coordinates of each cell, other parameters were also noted: color (belonging to the red or green subclone), morphology (neuron, astrocyte, or oligodendrocyte), spatial location (sSC, dSC and PAG visibly demarcated by DAPI signal). For population analysis, astrocytes were identified based on their distinct protoplasmic morphology and oligodendrocytes were labeled using anti-Olig2 antibodies to distinguish them from small neurons. All information were then stored in Microsoft Excel for further analysis. For the quantification of 3D parameters of clones, we determined a midline projecting through the reference point and the centroid of the clone. The maximum radial displacements of cells from the reference point in 3D were then calculated for each clone. Similarly, maximum tangential displacement of cells from the midline in 3D was also determined for each clone. The cell dispersion in each clone was calculated based on the standard deviation of each cell location in 3D. For MADM population analysis of Control-MADM and *Pten*-MADM tissues, cell counting was performed using a built-in plugin *Cell Counter*. The counts and x-y coordinates of red and green cells were exported to Microsoft Excel for further analysis.

RNA Sequencing Data Analysis

Embryonic scRNA-sequencing data analysis

Initial analysis, including integration was performed using R v4.1.2 and Seurat v4.1.0.[79]

La Manno et al. dataset: For the embryonic reference single-cell count data[23] was downloaded from https://storage.googleapis.com/linnarsson-lab-loom/dev_all.loom. Loom files were processed using loomR (0.2.1). Cells were retained based on the following annotations stored as column attributes: Tissue: Midbrain or MidbrainDorsal, Subclass contains: midbrain or mixed. For cells with Age e9.0, e10.0, e11.0 we retained cells with the following Location attributes: Caudal and dorsal midbrain (caudal m1A), Alar plate of the midbrain and diencephalon, Roof plate of midbrain, diencephalon and pallium, Midbrain-hindbrain boundary diffuse, Midbrain and diencephalon roof plate, Midbrain alar plate, Midbrain roof plate, subpallium ganglionic eminence, Midbrain diencephalon roof plate, Midbrain dorsal, hindbrain lateral, Midbrain. Class: Neuron, Neuroblast, Radial glia. A Seurat object was prepared with these cells using CreateSeuratObject with min.cells = 5, min.features = 500 parameters. We split this data by the Age attribute, normalised each dataset using NormalizeData with normalization.method = "LogNormalize", scale.factor = 10000 parameters and determined variable features using FindVariableFeatures with selection.method = "vst", nfeatures = 2000 parameters. *Pooled embryonic Fzd10-lineage dataset*: Initial analyses was performed using cellranger-7.0.0 with transcriptome version: mm10-2020-A, including intronic information. All downstream analyses were performed using filtered_feature_bc_matrix.h5 file from CellRanger. We created a Seurat object from this data using CreateSeuratObject with min.cells = 3, min.features = 200 parameters and retained only high quality cells based on these parameters: nFeature_RNA > 200 & nFeature_RNA < 6000 & percent.mt < 5. Normalisation and finding variable features was done as for the reference. All reference and the pooled embryonic *Fzd10*-lineage data were integrated using

SelectIntegrationFeatures, FindIntegrationAnchors and IntegrateData with default parameters. For downstream analyses we used the predictive power of the large, integrated dataset, if not stated otherwise. Visualizations focused on La Manno data only, to improve clarity of data presentation. All subsequent analyses were performed with R v4.2.1 and Seurat v4.2.0.

UMAP, cluster assignment: Initial clustering was performed using ScaleData, RunPCA (npcs = 30), RunUMAP (reduction = "pca", dims = 1:26), FindNeighbors (reduction = "pca", dims = 1:23), FindClusters (resolution = 1.8). We identified 2 clusters with low numbers of detected genes that were also disconnected from other cells on the UMAP. Cells from these 2 clusters were removed and the data re-clustered: RunPCA (npcs = 50, verbose = FALSE), RunUMAP(reduction = "pca", dims = 1:30), FindNeighbors (reduction = "pca", dims = 1:30), FindClusters(resolution = 0.2). Final clustering is visualised in Figure S1C.

Developmental trajectory: Figure S1B: Gene expression was visualized using FeaturePlot with order = T, min.cutoff = "q25", slot = "scale.data" parameters. Figures 1B, 1D, 1F, 1I: UMAPs show only La Manno et al. cells. Figure 1B: Colors were assigned based on the Class attribute. Note that Neuroblasts are labeled as Immature Neurons. Figure 1C: Relative abundances of La Manno et al. cells with a Class attribute were calculated at each available developmental stage. Note that Neuroblast was renamed to Immature Neurons. Figure 1D: Seurat clusters as shown in Figure S1C were assigned a cell type using cells from LaManno et al. and the corresponding Class and the Subclass attributes. Clusters assigned as Excitatory Neurons or Inhibitory Neurons were colored. Figure 1E: Relative abundances of La Manno et al. cells with a Subclass attribute containing glutamatergic (Excitatory Neurons) or GABA (Inhibitory Neurons) were calculated at each available developmental stage. Error bars for both figures were determined with clopper.pearson.ci (alpha = 0.05, CI = "two.sided") from GenBinomApps v1.2. Figures 1F and S1D: For monocle3 (v1.2.9)[80] analysis the Seurat object was converted using as.cell_data_set (SeuratWrappers v0.3.1), cells were clustered using cluster_cells and the trajectory graph was learned using learn_graph with learn_graph_control = list(ncenter=1000, nn.k=25, geodesic_distance_ratio=0.25, euclidean_distance_ratio=1.5), close_loop = T, use_partition = T parameters. Indicated start points of trajectories were defined manually using order_cells with reduction_method = "UMAP" parameter. *Inference of adult cell types*: Figures 1H, 1I and S1F: We extracted UMI counts of relevant cells from the adult mouse SC[24] and prepared a Seurat object as described for MADM-CloneSeq reference cells. Using this Seurat object we followed the standard workflow: NormalizeData, FindVariableFeatures (selection.method = "vst", nfeatures = 2000), ScaleData, RunPCA (npcs = 30), RunUMAP (reduction = "pca", dims = 1:20). The resulting UMAP is shown in Figure S1F. We reasoned that the latest embryonic time point (e18) will be most similar to adult cell types. Therefore we extracted raw UMI counts for e18.0 cells from the embryonic reference and performed the following processing workflow: CreateSeuratObject (min.cells = 3, min.features = 200), NormalizeData, FindVariableFeatures(selection.method = "vst", nfeatures = 2000). For label transfer, first transfer anchors were determined: FindTransferAnchors with dims = 1:20, reference.reduction = "pca". With these anchors label transfer was performed: TransferData (dims = 1:20). This analysis defines similarity scores for each e18 embryonic reference cell to each of the adult cell clusters. Note that we focused this analysis on neurons and thus excluded clusters 0, 6, 11 (Figure S1C) from this analysis. For Figure 1H we calculated the mean similarity score of embryonic reference cells in each Seurat cluster (Figure S1C) to each of the adult cell types. Heatmap of the resulting matrix was drawn using pheatmap (v1.0.12) with scale="row". Figure 1I: Finally, we inferred for each adult cell type the most likely cluster of origin in the embryonic data by the highest mean similarity score and visualised this association on the UMAP.

Fzd10-transgene characterization: Figures S2M–S2O: For QC plots we used nFeature_RNA as genes, nCount_RNA as transcripts. Figures S2Q–S2R: Number of cells from embryonic reference or from pooled embryonic *Fzd10*-lineage cells was counted in each Seurat cluster as shown in Figure S2Q (NOTE: only *Fzd10*-lineage cells are shown in this UMAP) and Figure S1C. Relative number of cells in each cluster were calculated and plotted. Pearson's product-moment correlation and p-value were calculated using cor.test function.

Glia analysis: We created a dedicated Seurat object from reference dataset as described above from LaManno et al., but focusing on cells with Class attribute: Radial glia and Glioblast. To determine glia progenitors in the pooled embryonic *Fzd10* cells, we re-analyzed the integrated reference and the pooled embryonic *Fzd10*-lineage data. Since glioblast cells were excluded from the reference in the initial analysis, we reasoned that glioblast cells from the pooled embryonic *Fzd10*-lineage data clustered with Radial glia cells. To identify these cells, we determined clusters with high expression of glia progenitor markers (*Aldh1l1, Sox9, Olig2, Olig1*) in the integrated data. Such analysis identified 4 clusters from which we specifically extracted the *Fzd10*-lineage cells and prepared a new Seurat object. Next we integrated reference data and pooled embryonic *Fzd10*-lineage using standard parameters as described above. Finally we performed ScaleData, RunPCA (npcs = 30) and RunUMAP (reduction = "pca", dims = 1:15) on the integrated data.

MADM-CloneSeq data anlaysis of E10 clones

Reference dataset: As a reference dataset we used published single-cell RNA-seq data[24] by downloading the raw read counts in loom format (https://storage.googleapis.com/linnarsson-lab-loom/l5_all.loom). All statistical analyses were performed in R v4.0.3.

Data alignment and read counting: We obtained single cell RNA-seq data from 429 samples containing 399 neurons and 30 negative controls. Negative controls contained sample collection solution (5% RNase inhibitor, 0.2% Triton-X RNase-free PBS) prepared on different days of experiment. Alignment was done using STAR (v.2.7.9a)[85] on GRCm39 and Gencode vM27 with STAR parameters: –outFilterMultimapNmax 1 –outSAMstrandField intronMotif –outFilterIntronMotifs RemoveNoncanonical. We retained 352 neurons with > 26000 unique aligned reads (median negative control: 26299.5) and >5% fraction uniquely aligned reads (median negative control: 2.3%). Reads in exonic and intronic regions (Gencode vM27) were counted using the aligned bam files produced by STAR and summarizeOverlaps (GenomicAlignments v1.26.0) with singleEnd=TRUE, mode = "IntersectionNotEmpty", ignore.strand = T, inter.feature = T parameters. TPM values were calculated separately for exonic and intronic regions using calculateTPM (package

scater v1.18.6).[81] Intronic and exonic TPMs for each gene were summed up, transformed as $\log_2$(TPM+1) and used for creating a Seurat (v4.0.4) object with min.cells = 5, min.features = 500 parameters.

Normalized Marker Sum (NMS) analysis: Using the reference dataset we extracted read counts from dorsal midbrain (Tissue = MBd) cells, removed cells with duplicated CellIDs and created a Seurat object with min.cells = 5, min.features = 500. Expression values were normalized (NormalizeData with normalization.method = "LogNormalize" and scale.factor = 10000 parameters) and scaled (ScaleData from Seurat package) using all genes. We identified top 200 marker genes for cell types from Taxonomy Rank 3 with more than 100 cells (Oligodendrocytes, Di- and mesencephalon neurons, Astroependymal cells, Vascular cells, Immune cells). Such analysis identified 986 unique genes (minimum of 188 genes per group). Next, we determined the highest expressing cell type for each marker gene to assign each gene to one cell type. We used the top 188 highest expressed genes for each group as marker genes to calculate the mean expression of cell-type marker genes in the corresponding cell type of the reference (mean expression value of all cells in the cell type). For each MADM-CloneSeq cell, the mean marker gene expression for each reference cell type was determined (5 expression values for each MADM-CloneSeq cell). Finally, we determined the NMS score for each cell type by dividing the mean marker gene expression in each MADM-CloneSeq cell by the mean expression of cell type in the reference. Note that the absolute gene expression levels of the reference and the MADM-CloneSeq cells were of a different scale due to the difference in the calculation of gene expression (TPM vs UMI counts). More specifically the MADM-CloneSeq TPM gene expression values were ~8x higher than the corresponding UMI counts in the reference. Since the NMS score is a direct comparison of reference / MADM-CloneSeq cells, we changed the neuron NMS cutoff from 0.4[97] to 3. We thus only retained MADM-CloneSeq cells with a neuron NMS score > 3 and the highest non-neuronal NMS score < 4 (312 neurons). Finally, we corrected for possible batch effects in the MADM-CloneSeq data using SCTransform with vars.to.regress = c("Plate", "STAR.perc") and residual.features = [all genes in expression matrix] parameters.

Data integration and cell-type assignment: From reference cells, we extracted 16 cell types (MEGLU1, MEGLU2, MEGLU3, MEGLU4, MEGLU5, MEGLU6, MEINH2, MEINH3, MEINH5, MEINH6, MEINH7, MEINH8, MEINH9, MEINH10, MEINH11, MEINH12) that were located in our region of interest based on the predicted positional location (http://mousebrain.org/development/celltypes.html). We extracted 3696 cells from these cell types (using column attribute ClusterName in the reference loom file) and created a Seurat object with min.cells = 5, min.features = 500 parameters. To prepare a reference UMAP we used SCTransform with standard parameters, RunPCA (assay = ‘‘SCT’’ parameter) and RunUMAP (dims = ‘‘1:20’’ parameters). For data integrations, reference data was processed using SCTransform with all genes of the count matrix as residual.features. Then we identified marker genes for each cell type using FindAllMarkers with logfc.threshold = 0.2 parameter. Top 100 marker genes for each cell type were determined and intersected with informative genes in the scale.data slot of the SCT assay of both reference and MADM-CloneSeq cells. Such analysis identified 996 genes that were used as features for data integration. For data integration we used the scale.data slot of the SCT assay by modifying the RunFastMNN function of the seurat-wrappers package. Note that RunFastMNN is a wrapper for the fastMNN function of the package batchelor (v1.6.3).[82] For cell type assignment we used the expression matrix reconstructed from the low-rank approximation from fastMNN integration (assay = "mnnreconstructed"). We calculated the median expression of the same 996 genes identified above to calculate the mean expression across all reference cells in each cell type (centroid). Then we determined the Pearson correlation and associated test statistic (function cor.test with alternative = "two.-sided", method = "pearson" parameters) of each MADM-CloneSeq cell to each centroid. Each MADM-CloneSeq cell was assigned the cell type to which it had the highest correlation (nearest centroid). To assess the robustness of the mapping we used bootstrapping over genes. We selected 100 bootstrap samples of 996 genes with replacement, performed the nearest centroid classification and calculated a score by determining the fraction of the cell-type assignment from bootstrapping analyses being identical to the cell-type assignment of the real data (bootstrap score). For final analysis we used MADM-CloneSeq cells with highest correlation > 0.1, a bootstrap score > 0.5 and that belong to a clone with >30% collected cells (253 neurons). See Table S1 for details on sample metadata.

UMAP visualization: To visualize MADM-CloneSeq cells on reference UMAP space we used a previously introduced pipeline[98] that uses Seurat as well as an R implementation of the UMAP library (https://github.com/tkonopka/umap) with modifications. Specifically, we used dimensionality reduction from fastMNN (first 25 dimensions) as well as the reference UMAP coordinates calculated above as an input into the UMAP pipeline.

Excitatory/inhibitory neuron marker analysis: Excitatory neurons were identified based on their respective cell types with excitatory neuron IDs starting with MEGLU and inhibitory neurons starting with MEINH. Note that for the sake of clarity we changed the cell-type IDs for the MADM-CloneSeq cells in the final figures. For an exchange table see Figure S1E. To identify differentially expressed genes (DEGs) between excitatory/inhibitory neurons in reference as well as MADM-CloneSeq data we used FindMarkers with parameter: logfc.threshold = 0.2. Genes were filtered for DEGs present in both analyses (reference and MADM-CloneSeq) and with an adjusted p-value < 0.01 in the MADM-CloneSeq data. A DE score was determined as the $\log_{10}$ of the adjusted p-value and corrected to be positive for genes with $\log_2$ fold-changes > 0. DE scores were cut at 5/-5 for better visualization, and plotted as a heatmap.

Cell-type marker analysis: We identified cell-type specific marker genes in both the reference and the MADM-CloneSeq data using FindAllMarkers with parameter: logfc.threshold = 0.2. We then determined the top 20 marker genes from the reference (ordered by average $\log_2$ fold-change) and intersected this gene list with the marker genes from the MADM-CloneSeq data. For heatmap visualization we prepared a differential expression score (DE score) by $\log_2$ transforming the raw p-value and correcting this value to be

positive for genes with a $\log_2$ fold-change > 0. This value was cut at 30 for MADM-CloneSeq or at 200 for reference data. In Figure S6I we used the whole gene list and for Figure S6J we arbitrarily selected specific genes for display.

Relative abundance of cell types: To test for differences in the relative distribution of cell types between *Fzd10*- and *Sox2*-clones we plotted the 95% Clopper-Pearson confidence intervals (function clopper.pearson.ci from the GenBinomApps package v1.1). Largely overlapping intervals indicated non-significant differences, which we confirmed using chi-square test with correction for multiple testing (all adjusted *p*-values = 1, function chisq.test with parameters: correct = F, rescale.p = F, simulate.p.value = T).

Cell-type pairing: To determine preferential pairing of cell-types in a single clone we compared the pairing frequency in the real data to a random dataset, where we permutated cell-type labels 10000 times, using z-scores, which we plotted as a heatmap. We determined p-values from z-scores using pnorm function and corrected for multiple testing. No corrected p-value was < 0.05.

Layer-specific cell-type distribution: To identify layer specific cell-type distribution we determined the number of neurons of each cell type in each layer (Subregion column of Table S1). To test difference to a random distribution we permuted the Subregion column 1000 times and calculated a z-score. The highest z-score for each cell type was used to calculate a p-value using pnorm function. To determine a random distribution of cell types in clones we considered hypothetical clones with 2, 3, 4, 5, 6, 7, 9, 10 and 12 cells. Then we randomly assigned one of the 16 cell types for each cell per clone. For each of these hypothetical clones we determined the number of unique cell types assigned to it. Randomization was done 1000x to calculate mean and standard deviation of unique cell types over all randomization. This data was used to draw the area of random distribution in Figure 4L as well as to calculate a z-score with associated *p*-value (using pnorm function). Note that after correction for multiple testing (p.adjust function with method = ''bonferroni'') all adjusted *p*-values = 1. For preparation of the cell-type linkage heatmap we determined a binary matrix indicating whether the respective cell type was assigned to one or more cells of the respective clone (black color) with rows representing cell types and columns representing clones. Heatmap and columns clustering was performed using pheatmap (v1.0.12) with parameters: clustering_distance_cols = "binary", clustering_method = "ward.D". Note that we restricted analysis for Figures S7N and S7O to 13 cell types with a significant association with a single layer. Figures S7K and S7O: AU (Approximately Unbiased) was determined using the same matrix as above using the pvclust package (v2.2.0, parameters: method.dist = "binary", method.hclust="ward.D", nboot = 10000). Note that an AU >95% is typically used to determine clusters that are strongly supported by data.[99]

MADM-CloneSeq data analysis of E12 two-cell MADM clones

Data alignment, NMS analysis, cell-type assignment and UMAP visualization was done as described for E10 MADM-CloneSeq data.

Random distribution of cell types in clones: We randomly assigned either exc/inh or one of the 16 cell types for each cell per clone. Randomization was done 10000x to calculate the mean and standard deviation of exc/inh neuron pairing or detection of distinct cell types. Exc/Inh pairing: Significance of difference to random data was determined using Chi-squared test for given probabilities (function: chisq.test with simulate.p.value = F parameter) using the following probabilities: exc only: 25%, inh only: 25%, mixed: 50%. Detection of distinct cell types: Significance of difference to random data was determined using z-score with associated *p*-value (using pnorm function).

Pten *scRNA-sequencing data analysis*

Reference data. For *Pten* control and *Pten* KO cell isolation, a *Nestin*-Cre driver[76] with broad expression (i.e. not specific to midbrain) was used. Therefore, we allowed for the possibility that the dissected midbrain contained ''contaminating'' cells from surrounding tissues, most likely hindbrain. To identify and remove non midbrain cells we established an embryonic reference following similar principles as described for Figure 1 but with different filters. We focused on e18 cells, since this age is closest to P0 data analyzed here. Specifically cells with Tissue tag Midbrain and Hindbrain as well as Age tag e18 were extracted. No other filters were used to allow for a broad annotation of cell types based on this embryonic reference. Workflow: CreateSeuratObject with min.cells = 5, min.features = 500 parameters. NormalizeData with normalization.method = "LogNormalize", scale.factor = 10000 parameters. FindVariableFeatures with selection.method = "vst", nfeatures = 2000 parameters.

Pten control and Pten KO cells: Data from sorted Control-MADM and *Pten*-MADM was processed using cellranger-7.0.0 with transcriptome version: mm10-2020-A, including intronic information. We created a Seurat object from the filtered_feature_bc_matrix.h5 file using CreateSeuratObject with min.cells = 3, min.features = 200 parameters and retained only high quality cells: nFeature_RNA > 200 & nFeature_RNA < 6000 & percent.mt < 5. Data normalization and variable feature detection was done for each of the 2 datasets as for the embryonic reference. Transfer anchors were determined between the embryonic e18 reference and the Control-MADM/*Pten*-MADM data using FindTransferAnchors with dims = 1:30 parameter. These anchors were used to transfer the Class and Tissue labels from embryonic e18 reference to Control-MADM/*Pten*-MADM cells using TransferData with dims = 1:30 parameter. For further analyses Control-MADM and *Pten*-MADM data was integrated using: SelectIntegrationFeatures, FindIntegrationAnchors, IntegrateData. Filtering steps: Starting number of high quality cells: 4212/4713 (Control-MADM/*Pten*-MADM). Remove cells with predicted Tissue hindbrain: 3049/1982. Remove cells with predicted Class Immune, Fibroblast, Vascular, Subcommissural organ, Blood: 2985/1889.

Further analysis: After filtering the combined Control-MADM/*Pten*-MADM data was further processed: ScaleData, RunPCA(npcs = 40), RunUMAP(reduction = "pca", dims = 1:35), FindNeighbors(reduction = "pca", dims = 1:35), FindClusters(resolution = 0.5). Figure 6O: UMAP with Class attribute as colors. Since Radial glia and Ependymal cells are likely producing glia cells at this developmental stage, we renamed these cell types as glia progenitors. Neuroblast was renamed immature neurons. Figure 6P: Cells with Class tag Neuron and Neuroblast were extracted and relative abundances calculated. Error bars were calculated as clopper.pearson.ci with alpha = 0.05, CI = "two.sided" parameters. Figure 6Q: Differential expression statistics were calculated using

FindMarkers ident.1 = Pten-MADM, ident.2 = Pten-Control, test.use = "MAST", logfc.threshold = 0.1 separately for neurons and neuroblasts/immature neurons. MAST was v1.22.0. DEGs were defined as adjusted p-value < 0.01 and avg_log2FC > 0 (up regulated) or avg_log2FC < 0 (down regulated). Figure 6R: Gene Ontology enrichment analysis of DEGs was performed with enrichGO (clusterProfiler v4.4.4) and OrgDb = org.Mm.eg.db (v3.15.0), ont = "ALL", readable = T parameters. The number of significantly enriched GO terms (adjusted p-value < 0.05) falling into 3 categories was determined, using the search pattern given in brackets: Interneuron (GABA|interneuron|inhibitory), Development (differentiation & neuron), Cell cycle (cell cycle). Figures S8D and S8E: DEG scores of genes mapping to one or more of the GO terms in the indicated group were determined as the $\log_{10}$ adjusted p-value. Prefix of the score was corrected to reflect direction of fold-change. Figure 6S: Cells with the Class tag Neuron were extracted and processed: ScaleData, RunPCA(npcs = 40), RunUMAP(reduction = "pca", dims = 1:30), FindNeighbors(reduction = "pca", dims = 1:30), FindClusters(resolution = 0.5). Actual UMAP with gene expression was prepared using FeaturePlot with features = c("Gad2", "Slc17a6"), blend = T, order=T, min.cutoff = "q10", max.cutoff = "q95", cols = c("#6d90ca", "#d8a428") parameters. Corresponding legend is shown in Figure S8H. Figures S8F and S8G: Cells were classified by investigating expression of 4 marker genes in the Seurat clusters. The association of Seurat clusters with excitatory (exc), inhibitory (inh) or mixed (exc/inh) cell type is as follows: 1: exc, 2:exc/inh, 3: exc, 4-7:inh. Figure 6T: Relative abundance of exc, inh and exc/inh cell types was calculated. Error bars were calculated as clopper.pearson.ci with alpha = 0.05, CI = "two.sided" parameters. Figure 6V: The combined embryonic pool/*Fzd10*-lineage data from Figure 1 was used as a reference to transfer the labels of the Seurat clusters as shown in Figures S1C and S2Q to Control-MADM and *Pten*-MADM data: FindTransferAnchors (dims =1:30), TransferData (dims=1:30). Note that we focused this analysis on clusters containing mainly neurons (excluding clusters 0, 6, 11). Based on this cluster annotation we calculated relative abundances separately for Control-MADM and *Pten*-MADM data and determined significance of difference between Control-MADM and *Pten*-MADM. Only clusters with significant differences are shown. All significances between relative abundances were calculated using chisq.test with correct = T, rescale.p = F, simulate.p.value = F and corrected for multiple testing using p.adjust with method = "BH" parameter. Stars: *** < 0.001, ** <0.01, * < 0.1.

Velocity analysis: For velocity analysis from Seurat object we used the embryonic data from this study (Figures S2I–S2O) and followed https://github.com/basilkhuder/Seurat-to-RNA-Velocity using velocyto v0.17.17[83] and scvelo v0.2.4.[84]

Statistical analysis

Data for clonal analysis, histological studies and MADM-CloneSeq documentations were stored and processed using Microsoft Excel (Microsoft). Statistical analyses were performed using GraphPad Prism software v8 (USA). All data were expressed as mean or median±standard error of the mean (SEM) or upper and lower limits where n represents the number of clones, unless otherwise stated. To test for normal distribution, Shapiro-Wik normality test was used. To test for statistical significance between two groups, either two-sided Mann-Whitney test or Student's t-test was used. To test for statistical significance between more than two groups, one-way ANOVA was performed with Dunn's multiple comparisons test between groups. Two-way ANOVA was used to compare the interactions between two sources of variations and to compare histogram distributions with Tukey's multiple comparisons test used to test between groups. When comparing changes in relative abundance across different conditions, Fischer's exact test or chi squared test was used. One phase decay exponential curve fit was performed to determine R^2 goodness of fit values. All explanations of n numbers, statistical tests used and p-values are detailed throughout results, STAR Methods or corresponding figure legends. Data for RNA-seq were processed according to description in STAR Methods sections and statistical details explained in results and corresponding figure legends.